Internal Waves and Turbulence in the Antarctic Circumpolar Current

STEPHANIE WATERMAN AND ALBERTO C. NAVEIRA GARABATO

National Oceanography Centre, University of Southampton, Southampton, United Kingdom

KURT L. POLZIN

Woods Hole Oceanographic Institution, Woods Hole, Massachusetts

(Manuscript received 25 October 2011, in final form 15 August 2012)

ABSTRACT

This study reports on observations of turbulent dissipation and internal wave-scale flow properties in a standing meander of the Antarctic Circumpolar Current (ACC) north of the Kerguelen Plateau. The authors characterize the intensity and spatial distribution of the observed turbulent dissipation and the derived turbulent mixing, and consider underpinning mechanisms in the context of the internal wave field and the processes governing the waves' generation and evolution.

The turbulent dissipation rate and the derived diapycnal diffusivity are highly variable with systematic depth dependence. The dissipation rate is generally enhanced in the upper 1000–1500 m of the water column, and both the dissipation rate and diapycnal diffusivity are enhanced in some places near the seafloor, commonly in regions of rough topography and in the vicinity of strong bottom flows associated with the ACC jets. Turbulent dissipation is high in regions where internal wave energy is high, consistent with the idea that interior dissipation is related to a breaking internal wave field. Elevated turbulence occurs in association with downward-propagating near-inertial waves within 1–2 km of the surface, as well as with upward-propagating, relatively high-frequency waves within 1–2 km of the seafloor. While an interpretation of these near-bottom waves as lee waves generated by ACC jets flowing over small-scale topographic roughness is supported by the qualitative match between the spatial patterns in predicted lee wave radiation and observed near-bottom dissipation, the observed dissipation is found to be only a small percentage of the energy flux predicted by theory. The mismatch suggests an alternative fate to local dissipation for a significant fraction of the radiated energy.

1. Introduction

Small-scale turbulence is thought to play an important role in the circulation of the Southern Ocean. The reasons for this are numerous. Turbulent mixing provides the dominant contribution to the downward buoyancy flux required to balance the upward diapycnal transport of deep waters implicated in the overturning circulation across the region (e.g., Lumpkin and Speer 2007; Zika et al. 2009; Naveira-Garabato et al. 2013). Turbulent kinetic energy dissipation acts as the ultimate sink for the energy input to the ocean by the wind, which is dominated by the wind work done on the Antarctic Circumpolar Current (ACC) (Wunsch 1998; Hughes and Wilson 2008; Scott and Xu 2009) and is also contributed to by work on upper-ocean inertial motions associated with variable wind forcing (Alford 2001; Watanabe and Hibiya 2002; Alford 2003; Furuichi et al. 2008).

While little certain is known on the physical pathway between large-scale energy input and small-scale turbulent dissipation in the Southern Ocean, the generation, propagation, and breaking of internal waves is believed to be centrally involved. In recent years, the potential importance of bottom-generated internal waves (forced by geostrophic and/or tidal flows impinging on rough topography) in particular has been discussed. Naveira-Garabato et al. (2004) and Nikurashin and Ferrari (2010a) pointed out the importance of turbulence ensuing from the breaking of internal waves generated as eddy flows impinge on rough sea floor

Corresponding author address: Stephanie Waterman, Climate Change Research Centre, University of New South Wales, Sydney, NSW 2052, Australia.
E-mail: snw@alum.mit.edu

DOI: 10.1175/JPO-D-11-0194.1

topography in the damping of the Southern Ocean's energetic mesoscale eddy field, although alternative mechanisms have been put forward [see section 5.3 of Ferrari and Wunsch (2009) for a review and Polzin (2010) for a specific example]. The topographic generation process has also been identified as a considerable player in the dynamical balance of the ACC (Naveira-Garabato et al. 2013) and, arguably, large-scale overturning. Overall, the common perception at present is that internal lee waves and turbulence arising from their breaking in the ocean interior are potentially significant processes in shaping the large-scale circulation of the Southern Ocean, its dynamics, and its sensitivity to changes in forcing. Nonetheless, evidence to date in support of this view is largely either indirect or highly inferential.

This evidence involves two distinct lines of research. One of them rests on the application of finescale parameterizations of the rates of turbulent kinetic energy dissipation ϵ and diapycnal mixing κ associated with internal wave breaking to observations of internal wave shear and density fine structure on vertical scales of O (10–100 m). The basic physical principle of the parameterizations is that internal wave breaking results from a downscale energy cascade driven by nonlinear wave–wave interactions. Studies using these techniques (e.g., Naveira-Garabato et al. 2004; Sloyan 2005; Kunze et al. 2006; Thompson et al. 2007; Wu et al. 2011) reveal that the ACC hosts an energetic internal wave field in regions of rough topography and predict elevated ϵ and κ values in those areas that are tentatively attributed to the breaking of internal waves generated by ACC–topography interactions. The second line of evidence stems from the application of internal wave radiation theory to observations of small-scale [O(1–10 km)] topographic roughness and near-bottom velocity and stratification data to estimate the rate at which energy (or momentum) is transferred from the ACC quasi-geostrophic flow to the internal wave field. These calculations (e.g., Nikurashin and Ferrari 2010b, 2011; Scott et al. 2011; Naveira-Garabato et al. 2013) endorse the notion of an energetic internal wave field in Southern Ocean regions of small-scale topographic roughness, and predict depth-integrated turbulent dissipation rates at least as high as those obtained by fine structure studies.

In this article, we investigate these preceding views on the significance of internal waves and turbulence in deep Southern Ocean circulation by analyzing the first extensive full-depth fine- and microstructure measurements of those phenomena in the ACC. The measurements were gathered as part of the U.K.–Australia Southern Ocean Finestructure (SOFine) experiment, an observational program seeking to understand the roles that small- and mesoscale physical processes play in the dynamical balances, overturning circulation, and water mass transformation of a major ACC standing meander north of the Kerguelen Plateau. Specifically, the objectives of this work are as follows:

(i) to characterize the intensity and spatial distribution of ϵ and κ in a dynamically important region of the ACC in which the current glaringly interacts with a major topographic obstacle; and
(ii) to assess the relationship between the observed turbulence and the region's internal wave field, and to explore the physical mechanisms underpinning such relationship.

This paper is organized as follows. In section 2, we introduce the experimental region, describe the SOFine survey observations and their basic processing, and characterize the regional environment using the SOFine survey data. In section 3, we describe the microstructure observations of ϵ, κ, and the depth-integrated dissipated power. In section 4, we describe the fine structure observations of the internal wave field, specifically the distributions of internal wave energy, frequency, and polarization, and their relation to the turbulent dissipation observed. In section 5 we explore whether the near-bottom signals in dissipation and internal wave properties are consistent with our expectations for internal lee waves, comparing theoretical predictions of the internal lee wave vertical wavelength (based on observed near-bottom flow and stratification) to the vertical scales of the waves observed, and an estimate of the lee wave energy radiation to observed levels of internal wave energy and dissipation. In section 6, we provide a summary, discuss implications of our results, and outline avenues for future work.

2. Data and analysis

The site selected for the SOFine study was the northern flank of the Kerguelen Plateau in the south Indian Ocean. Here two main fronts of the ACC form large standing meanders in climatological atlases and ocean circulation models alike (Sparrow et al. 1996; Sokolov and Rintoul 2009). It is a region of complex topography with topographic scales that span two aspects of the dynamical balance of the large-scale Southern Ocean circulation widely thought to be significant. As a prominent topographic obstacle in the path of multiple ACC jets, the plateau is expected to play a significant role in sustaining much of the large-scale topographic form stress required to close the ACC momentum budget in models (Gille 1997). At the

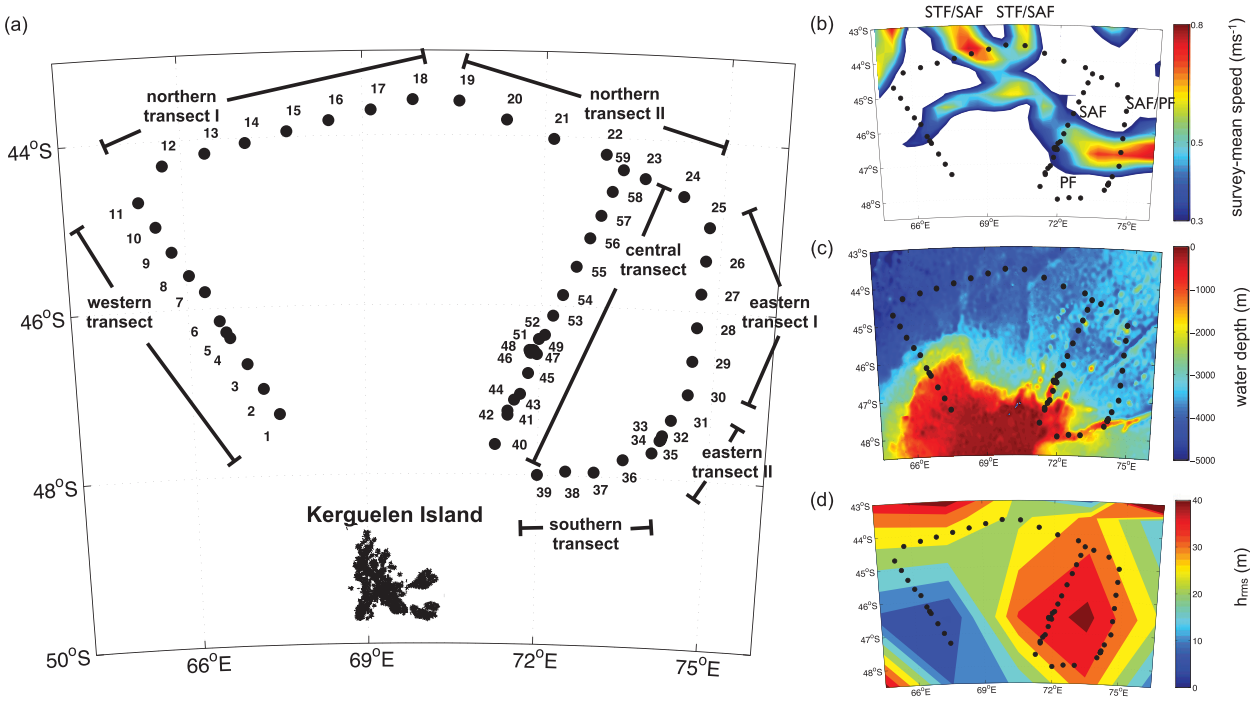

FIG. 1. SOFine survey stations and survey context in terms of ACC jet flows and bottom topography. (a) Location of SOFine survey transects and stations. (b) The survey-mean geostrophic surface flow speed in the region from Archiving, Validation, and Interpretation of Satellite Oceanographic data (AVISO) altimetry with the intersecting branches of the PF, SAF, and STF indicated. (c) Regional large-scale bathymetry at 1-min resolution from Smith and Sandwell ship-sounding bathymetry version 14.1 (Smith and Sandwell 1997). (d) An estimate of regional small-scale topographic roughness from Nikurashin and Ferrari (2011).

same time, as a volcanic ridge with small-scale [O(1–10 km)] topographic structure, the region may host elevated levels of internal wave activity and turbulence, generated as a consequence of strong quasigeostrophic flows impinging on the roughness of the plateau slopes (e.g., Nikurashin and Ferrari 2011; Scott et al. 2011; Naveira-Garabato et al. 2013). It should be noted however that regional estimates of topographic roughness at abyssal hill scales (1–10-km wavelength range) from Nikurashin and Ferrari (2011) are smaller by roughly a factor of 2 compared to those that characterize the Drake Passage, a site where elevated internal wave energy inferred turbulence and predictions for internal lee wave radiation have been reported by several past studies (e.g., Naveira-Garabato et al. 2004; Thompson et al. 2007; Nikurashin and Ferrari 2010b).

SOFine survey observations were collected in the region from the RRS *James Cook* in November and December 2008. The sampling of relevance to this article consisted of a double box survey defined by three sections emanating from the Kerguelen Plateau closed by a land boundary (Kerguelen Island) to the south and a perpendicular transect to the north of the plateau slopes (Fig. 1). At the time of the survey, these sections intersected various ACC frontal jets identified from temperature and salinity properties as branches of the Polar Front (PF), Subantarctic Front (SAF), a merger of branches of the SAF and the Subtropical Front (STF), and a merger of branches of the SAF and PF (G. Damerell 2012, personal communication). The survey consisted of a total of 59 stations separated by an average distance of 36 km with finer sampling over regions of steep topography and across fronts. Station measurements included simultaneous conductivity–temperature–depth (CTD) and lowered acoustic Doppler current profiler (LADCP) measurements, as well as free-falling vertical microstructure profiler (VMP) measurements, each sampling the full depth to within an attempted 10 m of the ocean floor. An altimeter on the lowered package permitted CTD and LADCP measurements to reach an accurate height of 10 m above the bottom. Preprogrammed weight-release depths for the VMP however could not be as accurate. Postprocessing shows that the deepest VMP measurements were on average ~30 m above the maximum CTD/LADCP depths, or ~40-m height above the bottom. The CTD used was a Sea-Bird 9/11 *plus* system. The LADCP package consisted of two RDI 300-kHz Workhorse ADCPs. The microstructure profiler used

was a full-ocean-depth Rockland Scientific International VMP-5500. CTD data were processed using Seabird software SBE data processing. LADCP data were processed both using the Visbeck software from the Lamont-Doherty Earth Observatory (Visbeck 2002) and the software originating from Eric Firing's group at the University of Hawaii, the former for estimates of absolute velocity and the latter for estimates of vertical shear. Microstructure processing was done by the authors using processing algorithms developed for the high-resolution profiler (Polzin and Montgomery 1996) modified to acknowledge the different sensor and noise characteristics of the VMP [see Waterman et al. (2012, manuscript submitted to *J. Phys. Oceanogr.*) for further details]. CTD processing provided vertical profiles of 2-dbar average temperature, salinity, oxygen, and pressure, while LADCP processing provided vertical profiles of 5- and 10-m average velocity for the University of Hawaii and Visbeck processing methods, respectively. Microstructure processing provided measurements of centimeter scale shear $\partial u/\partial z$ from which the dissipation rate of turbulent kinetic energy was estimated from $\epsilon = 15(\nu/2)(\partial u/\partial z)^2$. Here ν is the molecular viscosity and isotropy is assumed. For further details on CTD, LADCP, and VMP operations, calibration procedures, and initial CTD and LADCP data processing see Naveira-Garabato (2009). For further details on the VMP data processing see Meredith and Cunningham (2011).

A description of the regional environment in terms of potential temperature, salinity, neutral density, the background stratification, and flow speed as measured during the survey is given in Fig. 2. Note that here, and in following figures, fields are displayed as a function of depth and along-transect distance, and the section as shown starts in the southwestern corner of the survey domain, then runs clockwise along the rim of the survey, and finally northeastward along the central transect as illustrated in Fig. 1. Signatures of the PF jet are seen entering the survey area along the western transect over the steep plateau slope. Properties of merged branches of the SAF and STF are seen meandering in and out of the region on the northern boundary. Along the central transect, distinct branches of the PF and SAF are seen (the latter presumably an extension of the SAF entering the survey region from the northern boundary despite not being evident in the altimetry fields), while a broader jet with merged SAF/PF properties is seen to exit the region across the eastern boundary. Inside the core of these jets, speed as measured by the LADCP is enhanced throughout the water column. Jet speeds exceed 1 m s^{-1} in the upper ocean and are, on average, ~0.2 m s^{-1} averaged over the bottommost 500 m. The near-bottom speed reaches a maximum value of 0.33 m s^{-1} at station 30 where the SAF/PF exits the survey domain across the eastern transect.

3. Microstructure observations of turbulent dissipation and mixing rates

Here we present results related to the microstructure observations of the SOFine survey. We map the observed distribution of microstructure derived ϵ and κ and compute the depth-integrated dissipated power as a function of station. We consider these distributions relative to the regional environment, specifically the location of the ACC frontal jets and the nature of the small-scale topography.

Microstructure-derived measurements of ϵ show that, in general, our observations of the turbulent dissipation rates are highly variable (Fig. 3a), a variability that is likely due to the fact that the turbulence is both patchy in space and intermittent in time. The nature of the survey does not permit an evaluation of the influence of temporal variability on the patterns we observe; however, the correspondence of broad spatial patterns in turbulent dissipation and finescale properties (both internal wave energy discussed in section 4, and the dissipation rate predicted by a finescale parameterization discussed in the appendix) suggests that these patterns are, in many places, underpinned by spatial variability or variability on subinertial time scales. The interpretation of the observed patterns as spatial variability is further supported by the confirmation of many expected spatial patterns seen in the measurements. The observed turbulent dissipation rates tend to be generally elevated in the upper 1000–1500 m of the water column, and in some places near the bottom. In a regional mean sense, submixed layer enhancement exists in roughly the upper 1500 m of the water column with a maximum between 750- and 1000-m depth (Fig. 3b). Enhancement at the bottom exists in approximately the first 1000 m off the bottom and decays with height (Fig. 3c).

Despite these systematic patterns of enhancement however, overall the values of the dissipation rate we measure are moderate relative to our expectations for the ACC in regions of rough topography based on past studies (e.g., Naveira-Garabato et al. 2004; Sloyan 2005; Thompson et al. 2007; Zika et al. 2009; Naveira-Garabato et al. 2013). The overall regional (arithmetic) mean value of ϵ observed is 7.9×10^{-9} W kg^{-1} with a 90% confidence interval spanning 7.5×10^{-9} W kg^{-1} to 8.2×10^{-9} W kg^{-1}. (Here, and in all following mean and confidence interval estimates, means are arithmetic means and confidence intervals are calculated via a bootstrap method (Efron and Gong 1983) and

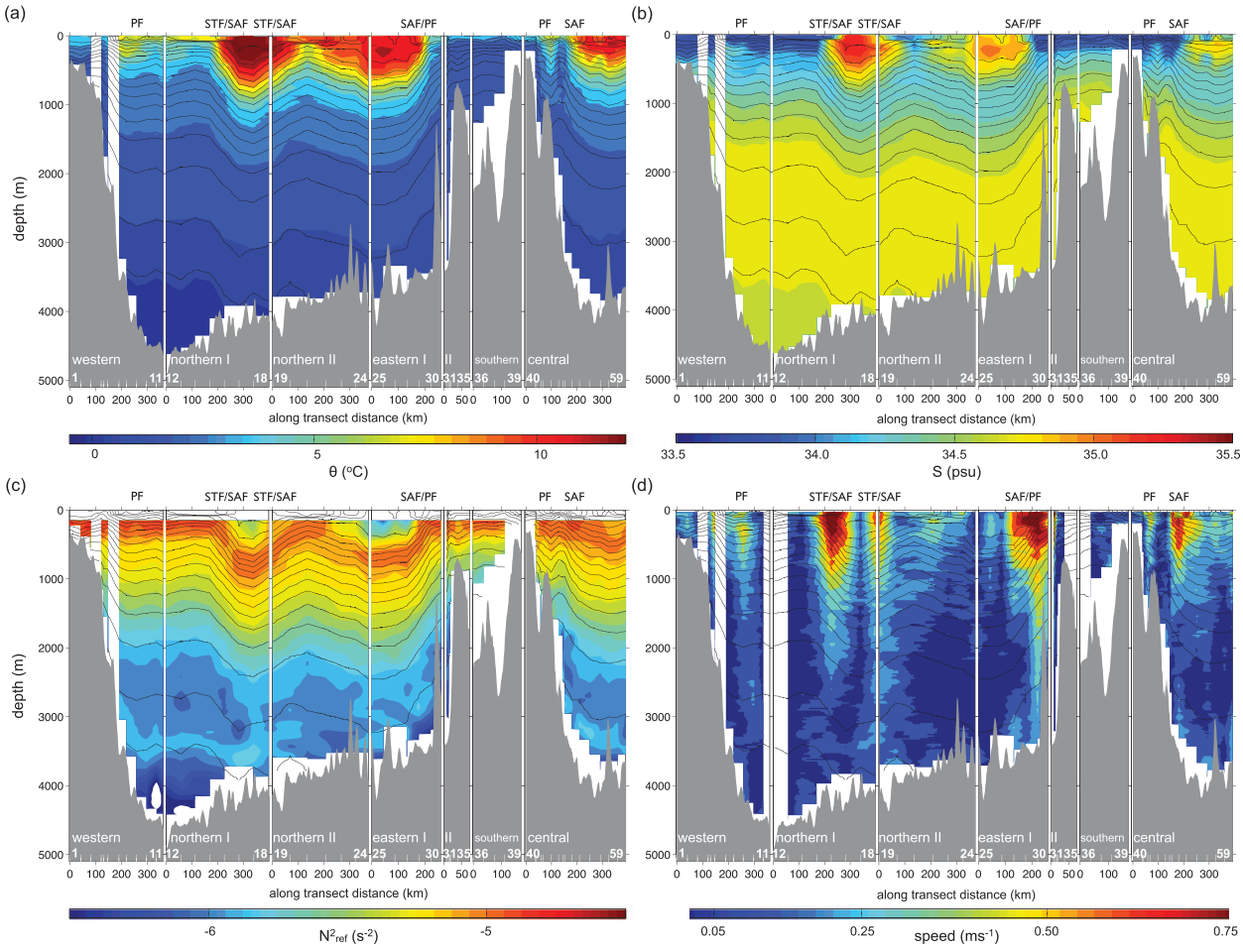

FIG. 2. Regional description of the SOFine survey environment: (a) potential temperature, (b) salinity, (c) background stratification (obtained by applying the adiabatic leveling method for calculating the buoyancy frequency of Bray and Fofonoff (1981) with a pressure range of adiabatic leveling of 400 db), and (d) speed as measured by the LADCP, each shown as a function of along-transect distance and depth. The section as displayed starts in the southwestern corner of the survey domain, then runs clockwise along the rim of the region, and finally northeastward along the central transect, with each subpanel corresponding to an individual transect as indicated. White ticks at the bottom of each panel delineate individual stations with key station numbers labeled to help orient the reader. Neutral density contours in the range of 26 to 28.4 kg m^{-3} in 0.1 kg m^{-3} intervals are shown in all panels by the black contours. Bottom topography is from Smith and Sandwell ship-sounding bathymetry version 14.1 (Smith and Sandwell 1997). The positions of the intersecting branches of the PF, SAF, and merged STF-SAF and SAF-PF are indicated above.

represent the fifth largest and smallest values of 100 sums formed by randomly sampling the data.) However this value is dominated by high values of dissipation in the surface mixed layer. In the ocean interior (here crudely approximated as below 250-m depth) the mean value is approximately an order of magnitude smaller. Interior upper ocean dissipation (between 250- and 1500-m depth) is characterized by a mean value of ϵ of 1×10^{-9} W kg^{-1}. Given the intermittent occurrences of elevated near-bottom dissipation, more meaningful average height profiles of the dissipation rate are those representing the average of stations with near-bottom ϵ enhancement versus a ''background'' profile. In the case of the former (the average of stations with a depth-integrated dissipation in the bottommost 1500 m greater than the regional mean value), the dissipation rate within 1500 m of the sea floor is characterized by an average value of ϵ of 2×10^{-9} W kg^{-1}. In contrast, the average height profile for the latter (the average of stations with a depth-integrated dissipation in the bottommost 1500 m less than the regional mean value) is characterized by an average value of 8×10^{-10} W kg^{-1} in the bottommost 1500 m. Estimates of mean values and their confidence intervals as a function of depth/height are displayed in the average profiles in Figs. 3b and 3c. We note the elevated dissipation rates at

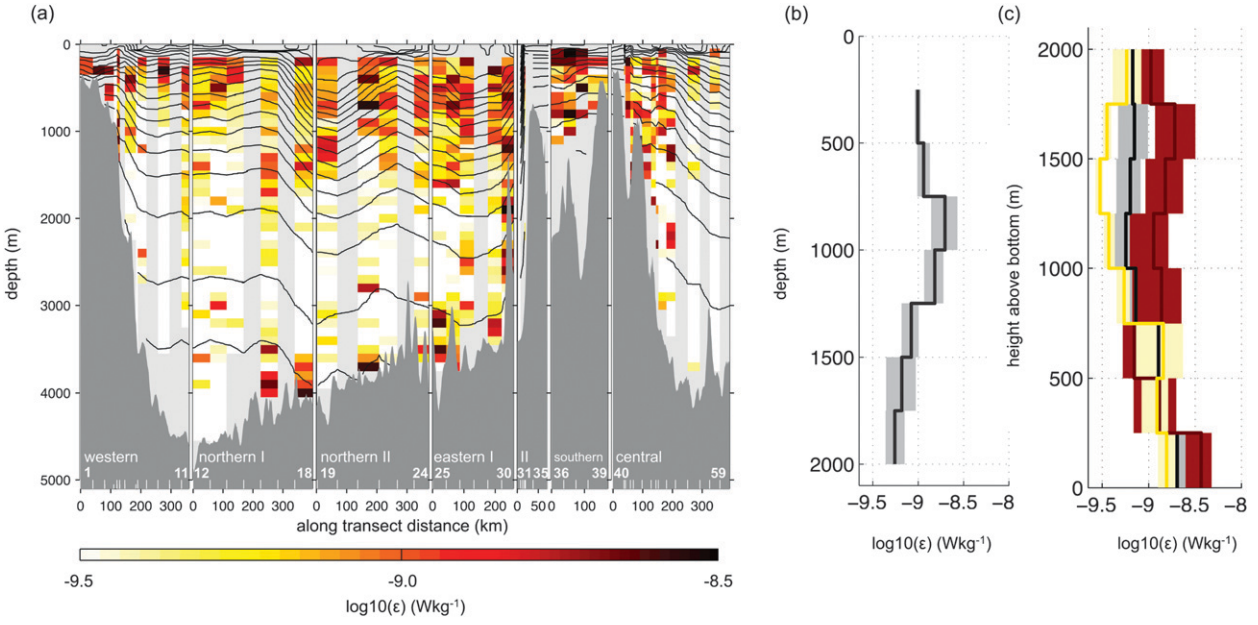

FIG. 3. Microstructure measurements of the turbulent kinetic energy dissipation rate ϵ. (a) An along-transect distance-depth section of $\log_{10}(\epsilon)$ displayed as in Fig. 2. The arithmetic mean profiles of ϵ as a function of (b) depth and (c) height above bottom. In (c) the overall mean profile (black) is contrasted with a mean profile for stations showing above average near bottom enhancement (red) versus those that do not (yellow) as defined in the text. The shaded area shows the 90% confidence interval calculated by bootstrapping. Note that here, and in following average vertical profiles, only stations of total depth greater than or equal to 2000 m are included to minimize the contamination of near surface with near bottom signatures.

~750–~1750-m height above bottom in the profile for stations showing enhanced near-bottom dissipation.

We translate the microstructure-derived value of ϵ into a turbulent mixing rate or diapycnal diffusivity κ using the Osborn relation $\kappa = \Gamma\epsilon N^{-2}$ (Osborn 1980). Here Γ is a mixing efficiency defined as the ratio between the buoyancy flux and the turbulent production, and N is the buoyancy frequency. Following Osborn (1980) we set Γ to 0.2. The resulting map and average vertical profiles of diapycnal diffusivity are shown in Fig. 4. Like ϵ, κ is highly variable. It is especially high in the vicinity of rough topography on the eastern side of the plateau (stations 31–51). Overall however, values of κ again are characterized as moderate relative to expectations for the ACC in regions of rough topography based on past studies, although they can be very high in some places. The overall mean ocean interior value (outside the upper 250 m) is 6.9×10^{-5} m^2 s^{-1} with a 90% confidence interval spanning 6.8×10^{-5} m^2 s^{-1} to 7.0×10^{-5} m^2 s^{-1}. The maximum interior value is two orders of magnitude larger. The average vertical distribution of κ (Figs. 4b and 4c) shows a small enhancement of the mixing rate with depth in the upper ocean, with the suggestion of a local maximum at approximately 1000-m depth (Fig. 4b). Here the average value of the mixing rate is 8×10^{-5} m^2 s^{-1}. Near the bottom, κ steadily increases toward the bottom reaching a maximum bottom 250-m-depth bin value of 2.0×10^{-4} m^2 s^{-1}. For stations characterized by above average near-bottom dissipation (as defined previously), this maximum value is 2 times larger and the average vertical profile shows a local maximum at ~1000–1250-m height. In contrast, the average ''background'' near-bottom value is half the overall mean value and shows no off-bottom enhancement.

We compute the depth-integrated interior dissipation from the microstructure measurements of ϵ and the CTD measurements of the density field. This dissipation is displayed in Fig. 5a. Values of turbulent kinetic energy dissipation excluding the upper 250 m are in the range of 0.7 to 13.5 mW m^{-2} with a regional mean value of 2.8 mW m^{-2}. As such, they are larger than the values in the southeast Pacific and smaller than those in Drake Passage inferred from the application of the finescale parameterization by Naveira-Garabato et al. (2004). They lie in between the fine structure inferred dissipation levels at 35°S and 55°S along I8S reported by Polzin and Firing (1997). In general, trends in the average dissipation along the various transects show similar trends to transect-average speeds and topographic roughness (Fig. 5d). Levels of dissipation are highest on the central and eastern transects where both depth-

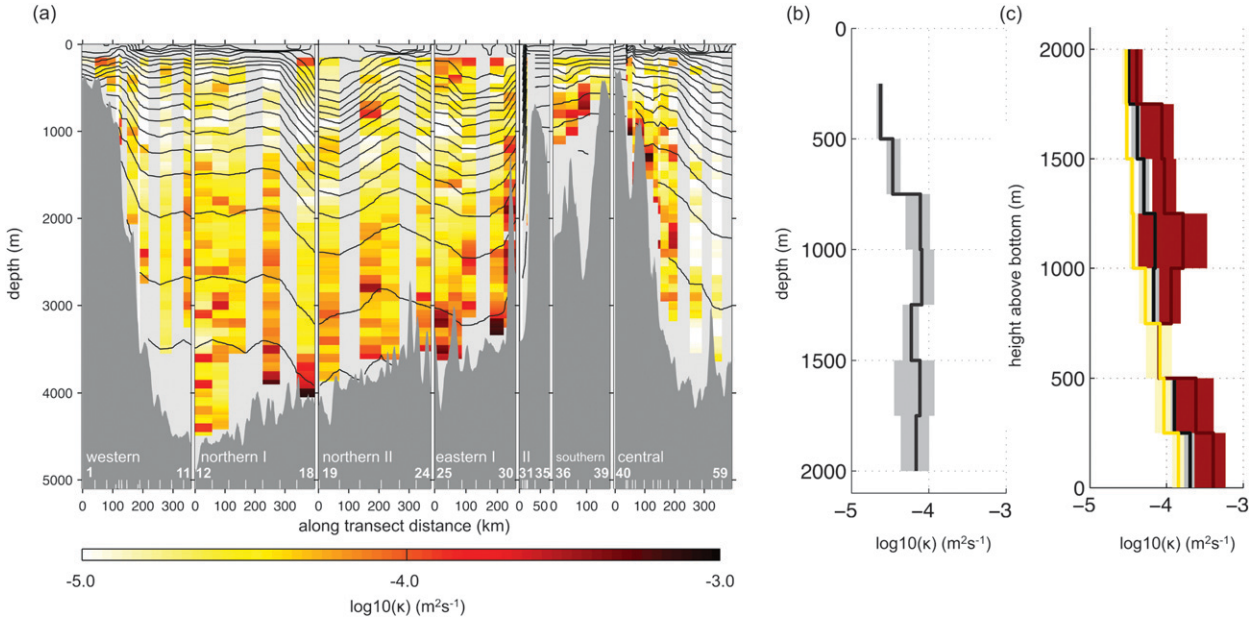

FIG. 4. Microstructure measurements of the turbulent mixing rate κ as displayed in Fig. 3.

averaged speeds and small-scale topographic roughness $h_{\rm rms}$ are often high. Levels are low along the western transect where $h_{\rm rms}$ is small. A station-by-station examination reveals that small $h_{\rm rms}$ values (<25 m) are always associated with small depth-integrated dissipation values (<4 mW m^{-2}), and that the largest observed depth-integrated dissipation values (>4 mW m^{-2}) are always associated with large $h_{\rm rms}$ values (>25 m); however, there are also many stations with rough topography ($h_{\rm rms} > 25$ m) and strong background flow speeds (depth-averaged speed > 0.1 m s^{-1}) that have weak dissipation. Temporal intermittency, time dependence, horizontal advection, and the dependence of lee wave energy radiation on the orientation of the flow relative to the topography, all may contribute to examples where rough topography and strong background flows do not equate to large dissipation rates. Of course, turbulent dissipation from other sources besides bottom-generated waves could also result in the realization of the counterexamples observed.

The correspondence between near-bottom dissipation (depth-integrated dissipation in the bottommost 1000 m), near-bottom flow speed, and topographic roughness is visualized in Fig. 6. Here we see that the highest near-bottom dissipation observed is associated with large $h_{\rm rms}$ values ($h_{\rm rms} \geq 30$ m) and large near-bottom flow speeds ($U_{\rm bot} \geq 0.2$ m s^{-1}), and near-bottom dissipation rates tend to be elevated in association with large topographic roughness. A station-by-station analysis reveals that almost all stations showing large near-bottom dissipation (>1 mW m^{-2}) are associated with relatively rough bottom topography ($h_{\rm rms} > 25$ m). The one exception (station 4) has a large near-bottom flow speed ($U_{\rm bot} = 0.17$ m s^{-1}). Again, however, there also exist examples where both the topography is relatively rough ($h_{\rm rms} > 25$ m) and the bottom flow is relatively strong ($U_{\rm bot} \geq 0.2$ m s^{-1}), and yet the near-bottom dissipation is relatively modest (<1 mW m^{-2}). Again temporal intermittency, time dependence, horizontal advection, the dependence of lee wave energy radiation on the orientation of the flow relative to the topography, and sources of turbulence other than breaking bottom-generated waves could result in these observations that do not show the expected dependence. It also should be noted that, owing to the relatively small number of stations, the large range of environmental conditions sampled, the dependence of lee wave radiation on multiple variables (i.e., bottom roughness, bottom flow speed and bottom stratification), and the temporal intermittency of turbulence, trends we identify are not statistically robust and remain inconclusive.

4. Relation to fine structure observations of internal wave properties

We test the hypothesis that internal waves play a central role in driving the turbulent dissipation observed by considering the observed maps of turbulent dissipation and mixing in the light of knowledge of properties of the regional internal wave field. Fine structure measurements consisting of CTD and LADCP

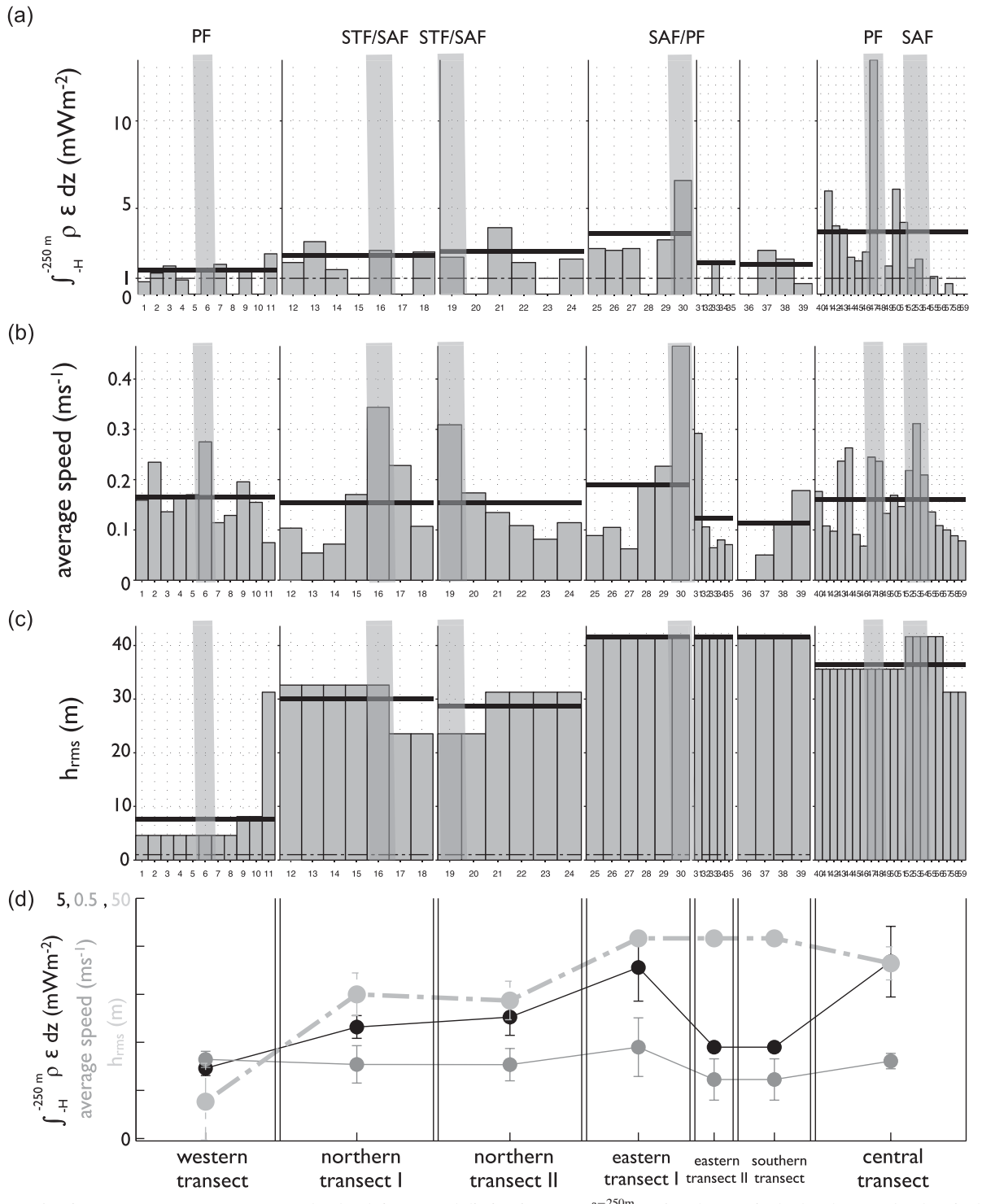

FIG. 5. Microstructure measurements of the depth-integrated dissipation rate, $\int_{-H}^{-250\mathrm{m}} \rho\epsilon\, dz$, where H is the local water depth, ρ is the water density, and z is the vertical coordinate, and its relation to background flow speed and bottom roughness. (a) Microstructure measurements of the depth-integrated dissipation per unit area as a function of station. The dash-dotted line indicates the expected level for the canonical Garrett–Munk (GM) internal wave field [$\rho_o \int_{-H}^{0} \epsilon_0\, dz \sim 1\,\mathrm{mW\,m^{-2}}$]. (b) Depth-averaged speed as a function of station as measured by the LADCP. (c) Topographic roughness as a function of station as computed and reported in Nikurashin and Ferrari (2011). In each, the thick black horizontal line shows the transect-mean value. The vertical gray bars indicate the approximate positions of the various fronts intersecting the transects as labeled above. (d) A comparison of the transect-mean values of the above quantities: the depth-integrated dissipation rate (black solid line), depth-averaged speed (dark gray solid line) and topographic roughness (light gray dash-dotted line). Error bars indicate the standard error in the mean.

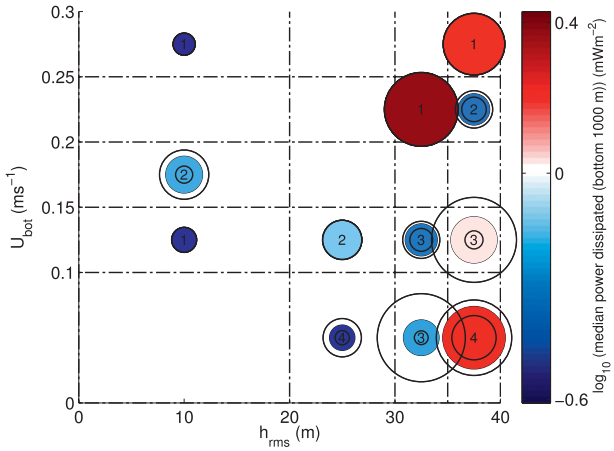

FIG. 6. Bin-average depth-integrated dissipation rates in the bottommost 1000 m as a function of bottom roughness and near-bottom background flow speed (average LADCP speed in the bottommost 500 m). Both the size and color of the dot display the median power dissipated. Black circles indicate the 90% confidence intervals on the median power computed via bootstrap sampling. The number inside the circle indicates the number of estimates in each bin.

profiles of temperature, salinity, and velocity permit a characterization of the regional velocity, shear, and strain fields on internal wave vertical scales. From these quantities, one can gain insight into characteristics of the regional internal wave field.

The regional map of internal wave energy (given by the sum of horizontal kinetic energy and potential energy, see the appendix for further details) integrated over a range of vertical wavelengths typical of internal wave scales is shown in Fig. 7a. Here energy is integrated over vertical wavelengths between 130 and 320 m that are well resolved by the fine structure measurements; however, patterns are robust for other reasonable wavelength range choices—again see the appendix for further details. Like the turbulent dissipation rate, internal wave energy is high in the upper 1000–1500 m of the water column, and in some places near the bottom, places often associated with rough topography (e.g., stations 24–27 and stations 36–42) and/or the ACC jets (e.g., stations 6–7, 16–20, 30, 45–47, and 54). Similarly, the station-averaged depth and height profiles (Figs. 7b and 7c) show enhancement in the upper 1000–1500 m and within 1000–1250 m from the bottom. Worthy of note is a pronounced local maximum at 1000–1500 m height in the average vertical profile characterizing stations with enhanced near-bottom dissipation. The correspondence of elevated turbulent dissipation with elevated energy at these vertical scales suggested visually by the spatial distributions of these quantities (Fig. 3 versus Fig. 7), is seen directly in an examination of the local relation between internal wave energy and turbulent dissipation (Fig. 8) and indicates a physical link between turbulent dissipation and the internal wave field at these scales. The role of internal waves in underpinning the near-bottom enhanced dissipation signals is suggested by the marked increase in near-bottom internal wave energy for stations with near-bottom ϵ enhancement (Fig. 7c, contrast the average height profile of internal wave energy for stations with enhanced near-bottom dissipation *vs.* stations representing background levels as defined in section 3), while the importance of bottom-generated waves as a source of this elevated near-bottom internal wave energy is suggested by the association of elevated near-bottom internal wave energy levels with elevated bottom roughness and bottom flow speeds (Fig. 9). Internal wave energy is consistently small in regions of smooth topography, and elevated values are consistently found in regions of relatively rough topography. Again however, like near-bottom dissipation, many instances of weak near-bottom internal wave energy levels in locations with relatively rough topography and strong near-bottom flow are also observed.

We make characterizations of the bulk frequency content of the internal wave field and the predominant direction of the internal wave energy flux by considering the shear to strain variance ratio R_ω and the ratio of counterclockwise to clockwise polarized shear variance (the ''polarization ratio'').[1] While the two-dimensional maps of both quantities (Figs. 10a and 10b) are noisy, there is a visual suggestion that strong polarization with a value of the polarization ratio greater than one (suggesting an elevated presence of downward-propagating internal waves) tends to occur in the upper ocean, and strong polarization with a value of the polarization ratio less than one (suggesting an elevated presence of upward-propagating internal waves) tends to occur close to the bottom. Similarly the map of R_ω suggests a tendency for the largest values of R_ω to be found in the upper 1000–1500 m (suggesting an elevated presence of near-inertial frequency waves there) while the lowest values (indicative of the dominance of waves with suprainertia frequencies) tend to be observed close to the bottom.

[1] See the appendix for definitions and details of their calculation from the observational data. Here again the range of vertical wavelengths considered in the variance integrals is from 130 to 320 m. Patterns are generally qualitatively similar for other ranges of suitable vertical wavelengths as well, however, R_ω (and in particular the strain variance) is very sensitive to the wavelength limits of integration.

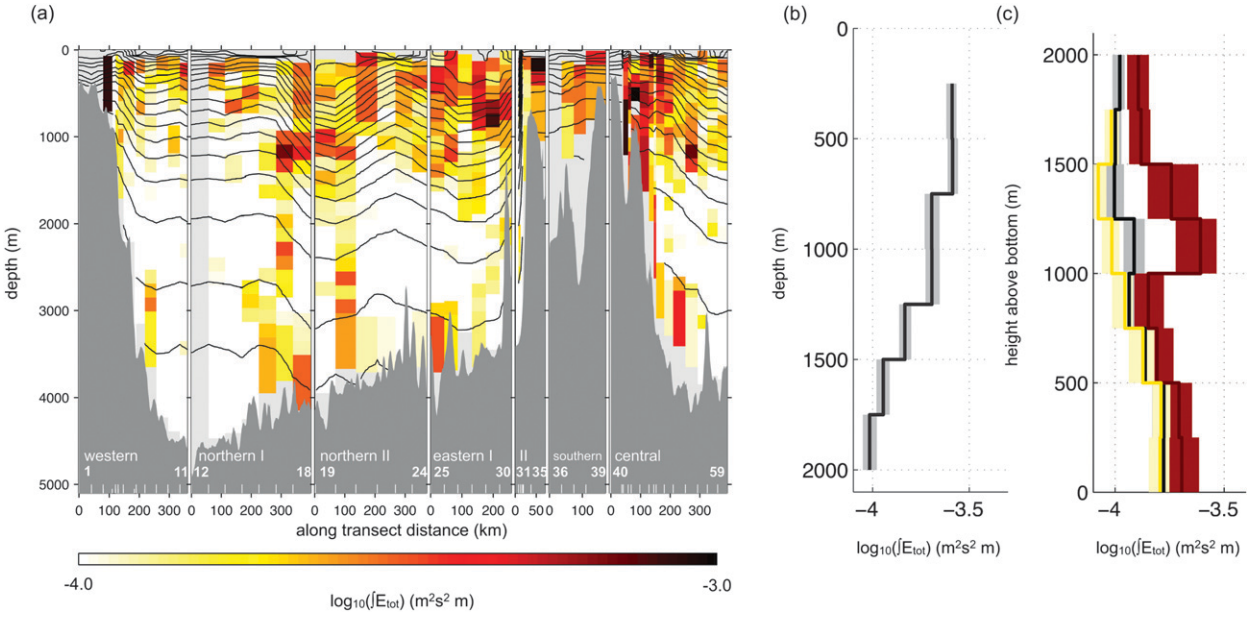

FIG. 7. Fine structure measurements of internal wave band total (horizontal kinetic + potential) energy integrated over a typical internal wave band vertical wavelength range (here 130–320 m). Display is as in Fig. 3.

Average vertical profiles as a function of depth and height above bottom (Fig. 11) in many cases confirm this characterization: near-inertial wave frequencies (as diagnosed from R_ω) tend to be found in the upper 1500 m and higher wave frequencies tend to be found in the bottommost 1500 m, while strong polarizations consistent with predominant downward energy propagation (polarization ratio large and positive) tend to be found in the upper 1500 m, and polarizations consistent with upward energy propagation (polarization ratio negative) tend to be found within 1250 m of the bottom for stations with significant near-bottom flow speeds. Predominant downward-directed energy propagation and near-inertial frequency content in the upper half of the water column are consistent with the picture of wind-generated near-inertial waves propagating downward from the surface into the interior, while predominant upward-directed energy propagation and suprainertial frequency content in the vicinity of the bottom are consistent with the presence of bottom-generated waves propagating upward into the interior. As such these patterns give insight into possible sources of internal wave energy and pathways of internal wave evolution in the region. In accord with this latter picture, we note that upward propagation and/or lower R_ω values (indicating higher-frequency waves) are especially prominent in the vicinity of the rough topography of the plateau and its slopes and in regions of strong bottom flow associated with the ACC jets (stations 6–7, 24–27, 36–42, 49–51, and 54) (Fig. 10).

Further insight into the pathways of internal wave evolution and potentially their relation to the generation of enhanced turbulent dissipation is suggested by contrasting the vertical profiles of these visualizations of internal wave frequency and energy propagation inside versus outside the ACC frontal jets and in the vicinity of strong versus weak bottom flows (Fig. 11). Here stations are grouped into one of two groups based on the magnitude of their mean speed in the upper 1500 m (to define "inside jets" versus "outside jets") and in the bottommost 500 m (to define "stations with strong bottom flows" versus "stations with weak bottom flows"). In each

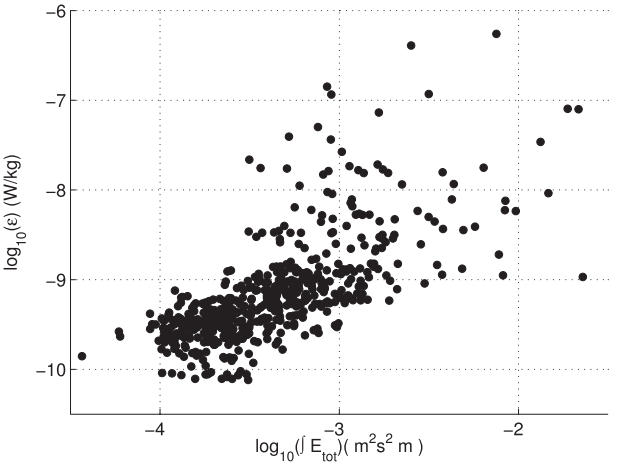

FIG. 8. The relation between integrated internal wave energy versus ϵ computed/averaged in 640-m-depth bins.

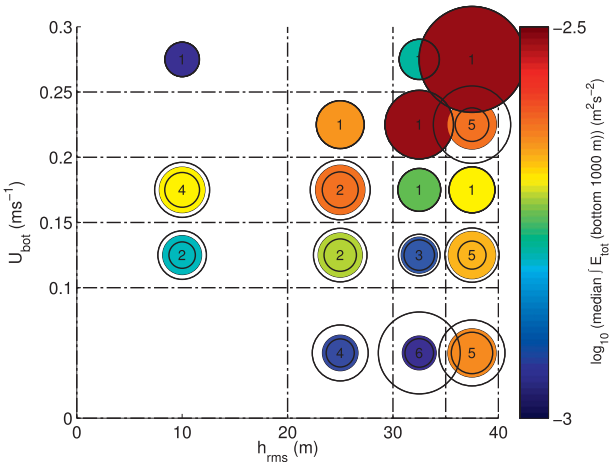

FIG. 9. Relation between bottom roughness, bottom flow speed, and near-bottom internal wave energy defined as the sum of the internal wave band total energy in the bottommost 1000 m. Display is as in Fig. 6.

case, stations with speeds greater than the regional mean value are included in the former grouping while stations with speeds less than the regional mean value are included in the latter grouping. The comparison illustrates several features of note that give potential insight into wave evolution. First consider the increasing tendency of R_ω with depth to a local maximum around 1250–1500-m depth (Fig. 11b). This tendency, consistent with a decrease in average wave frequency with depth, is consistent with the expected evolution of wave frequency for waves propagating downward into critical layers at middepths. The critical layers could arise either from the interaction of the waves with the background vertical shear resulting in a redistribution of wave energy to larger vertical wavenumbers or from vertical trapping because of the vertical variation of the background horizontal shear/geostrophic vorticity (e.g., Kunze 1985). Unfortunately, a lack of information on the vertical variation of the large-scale horizontal flow gradients make an assessment of the latter contribution difficult. An increase in the average polarization ratio between 500- and 1500-m depth and the sharp reduction of its value below, and the amplification of this pattern in the mean profile of stations inside jets relative to that of stations outside jets (Fig. 11c), is further consistent with the scenario of middepth critical layer fates for downward-propagating waves, as this pattern is consistent with an amplification of downward-propagating wave amplitudes around critical layer depths in the range of 500–1500-m depth and the relative reduction of the predominance of downward-propagating waves below. The near-bottom low R_ω signal is amplified in the mean profile of stations with strong bottom flows (Fig. 11e), suggesting waves generated by bottom flows may underpin the low R_ω/high wave frequency signal. An increase in the average R_ω value at 750–1000-m height above bottom, amplified in stations with strong bottom flows, suggests a localized decrease in average wave frequency at this height, consistent with the existence of critical layers for upward propagating lee waves. The existence of critical layers at this height for upward-propagating waves oriented into the flow is also suggested by the background flow profile characterizing stations with strong bottom flows (Fig. 11d), as the large-scale flow is observed to decrease with height above bottom to approximately 1000-m height. As such, in the bottommost 1000 m we expect wave–mean interactions to redistribute wave energy to larger vertical wavenumbers for lee waves propagating into the flow. The absence of a clear polarization consistent with upward energy propagation for stations with strong bottom flows above 1250 m (Fig. 11f) further supports the hypothesis that critical layers at approximately 1000-m depth may be a fate for upward-propagating lee waves. Consideration of the observational evidence of near-bottom critical layers that is tentatively suggested by these average profiles is currently underway.

We attempt to unite this picture of the regional internal wave population in terms of the sources of internal wave energy and pathways of internal wave evolution with the observed turbulent dissipation by considering average turbulent dissipation on an internal wave frequency-polarization map (Fig. 12). Again, confidence is limited by our failure to adequately sample the statistics of the phenomenon; however, despite this, there is a suggestion that the highest dissipation values observed are associated with waves of these two identified groups: high-frequency upward-propagating waves (polarization ratio < 1) and near-inertial waves propagating downward (polarization ratio > 1). The relative absence of high-frequency waves with downward polarization illustrates the tendency of downward-propagating waves to have near-inertial frequencies, consistent with the hypothesized wind-driven source. We note that this visualization illustrates that the upward-propagating waves we observe have a wide range of frequencies spanning 1–3f, where f is the inertial frequency.

5. Near-bottom signals and their relation to stationary lee wave theory

Finally, we examine the near-bottom signals in internal wave properties and turbulent dissipation and consider them in the context of stationary internal lee wave theory.

First we calculate the predicted lee wave vertical wavelength λ_z from stationary lee wave theory based

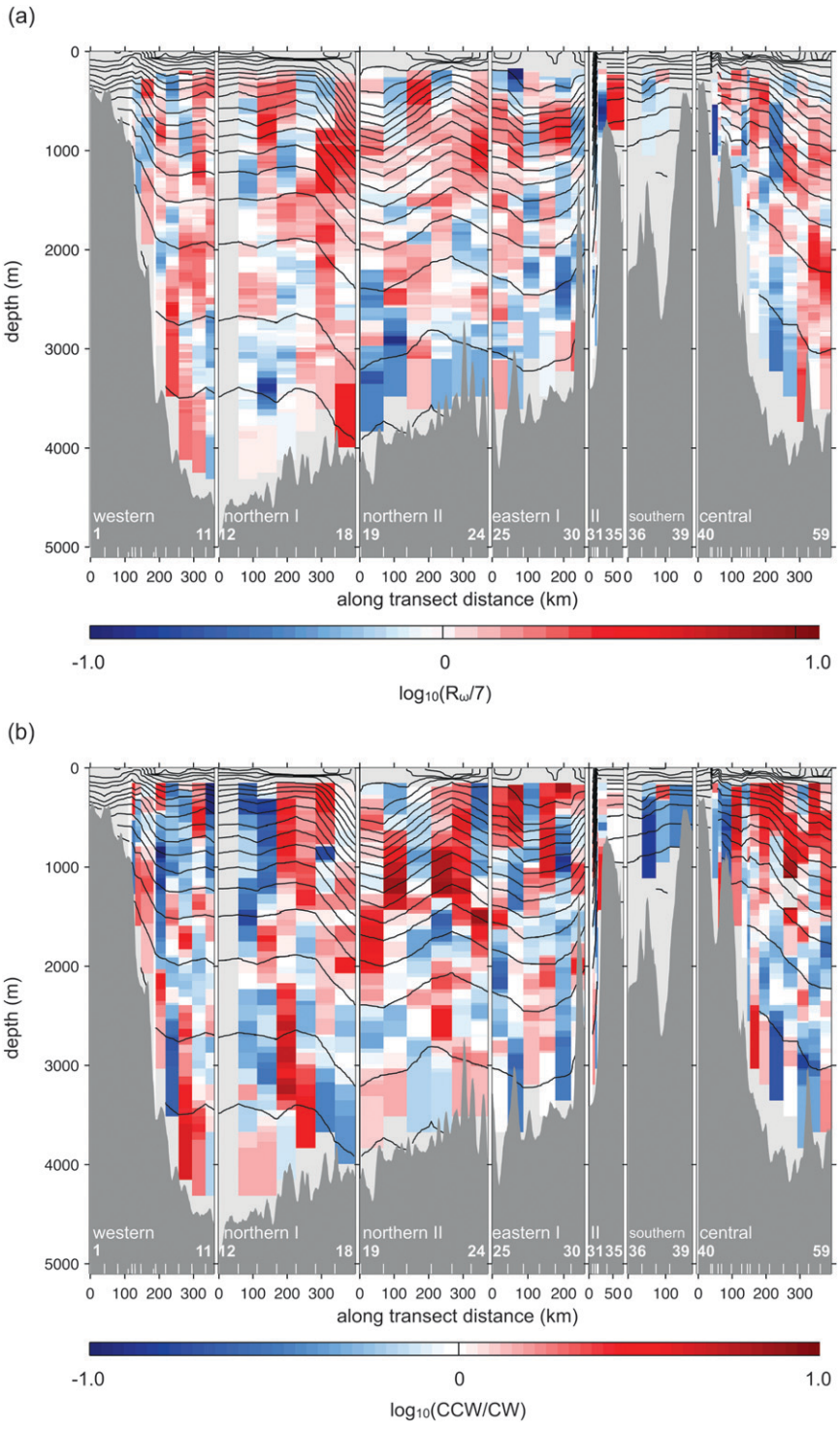

FIG. 10. An along-transect distance–depth section of (a) the logarithm of R_ω normalized by 7, the oceanic average value reported by Kunze et al. (2006), and (b) the logarithm of the polarization ratio. The sections are displayed as in Fig. 2.

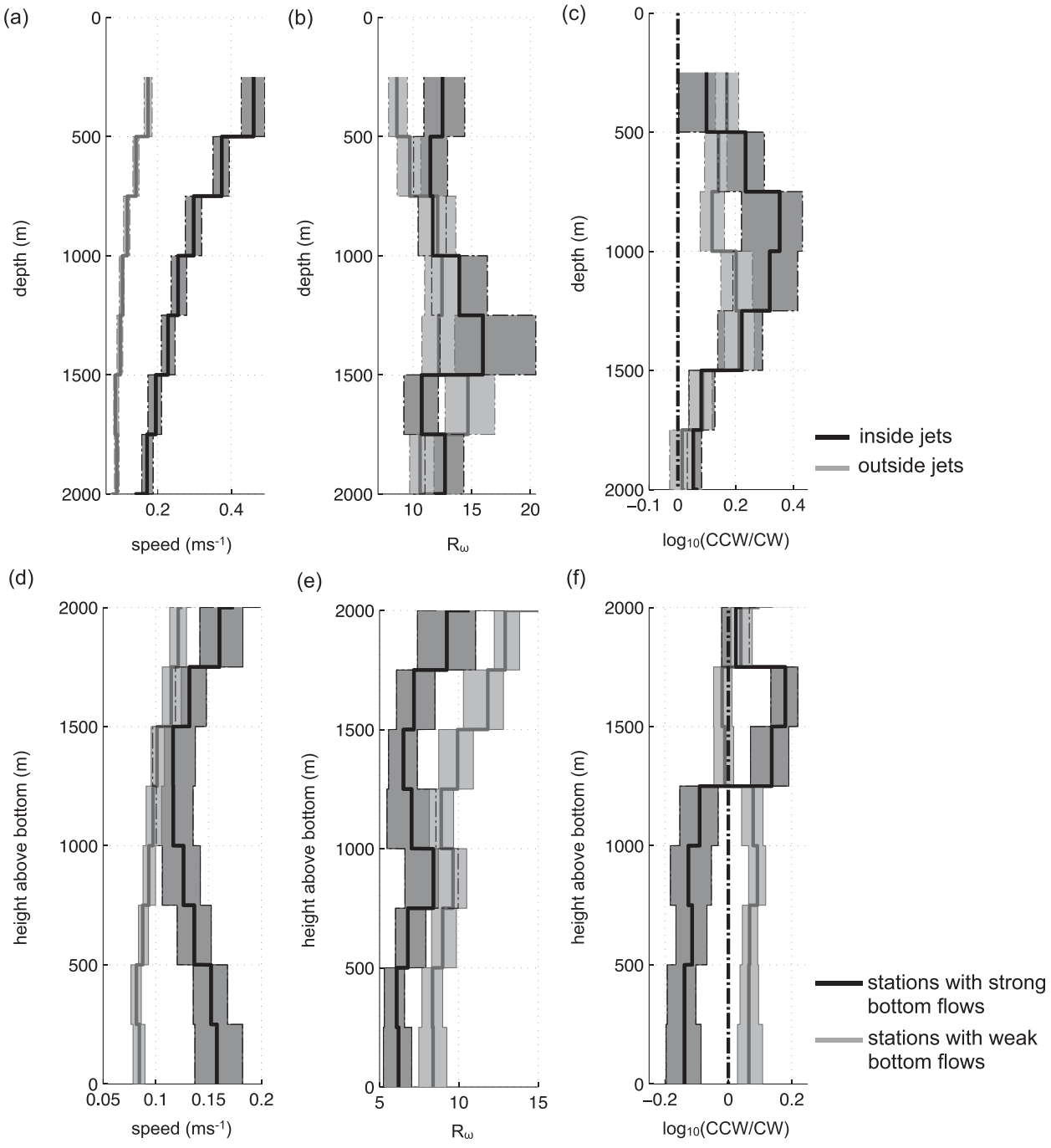

FIG. 11. Vertical profiles of (left) LADCP speed, (middle) R_ω, and (right) the polarization ratio as a function of (top) depth and (bottom) height above bottom contrasting the average of stations inside ACC frontal jets versus outside ACC frontal jets, and of stations with strong bottom flows *vs*. stations with weak bottom flows. Gray shading indicates the 90% confidence interval in the average vertical profiles calculated by bootstrapping.

on the observed bottom speeds $U_{\rm bot}$ and stratifications $N_{\rm bot}$, $\lambda_z = 2\pi U_{\rm bot}/N_{\rm bot}$ (Fig. 13). Bottom speeds and background bottom stratifications are estimated with the LADCP and CTD data and are defined as averages over the bottommost 500 m. The choice of this averaging scale is somewhat problematic: we seek to filter out internal wave signals [which, as will be seen, can have O(1000 m) vertical scales] and yet retain a characteristic representation of near-bottom values avoiding contamination from geostrophic shear.

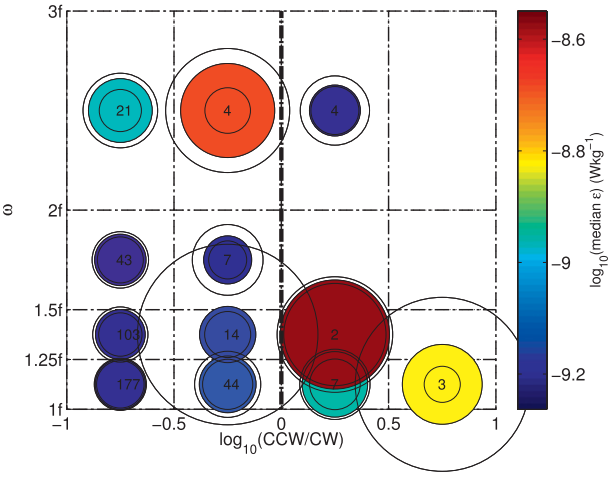

FIG. 12. Relation between bulk wave polarization, frequency (diagnosed from R_ω as $\sigma = \sqrt{(R_\omega + 1)/(R_\omega - 1)}f$ where f is the inertial frequency), and turbulent dissipation. Display is as in Fig. 6.

Potentially as a consequence, results of our calculations are often very sensitive to its choice. Here we consider 500 m following Nikurashin and Ferrari (2011), thus making our results comparable to theirs. Using this definition, bottom values of stratification N_{bot} are found to range from 1×10^{-3} s^{-1} in the deep waters north of the plateau to $\sim 4 \times 10^{-3}$ s^{-1} in the shallow waters on the plateau (Fig. 13b). Bottom speeds U_{bot} are much more variable. They tend to be largest in the shallow waters on the plateau and inside the ACC frontal jets: the average of this latter group is 0.19 m s^{-1} and the maximum (at station 30) is 0.33 m s^{-1} where the SAF/PF exits the survey domain along the eastern transect (Fig. 13a). Off the plateau and outside the ACC jets, bottom velocities are smaller: 0.07 m s^{-1} on average. The dependence of the predicted lee wave vertical wavelength on U_{bot} and N_{bot} implies that the largest predicted lee wave wavelengths are inside the ACC jets, where they are on the order of 1000 m on average, reaching a maximum of over 2000 m inside the SAF/PF crossing the eastern transect. Outside the ACC fronts, the predicted wavelengths are smaller: approximately 400 m on average. Predictions in the lee wave wavelength tend to track variations in the bottom speed field. We note that these large theoretical predictions, in particular at stations with strong bottom flows, are typically an order of magnitude larger than the vertical scales we are considering in our internal wave characterizations, and hence the scale of waves we have identified as showing enhanced near-bottom internal wave energy at these locations and signatures in their shear-to-strain and polarization ratios consistent with upward-propagating bottom-generated waves. The examination of internal wave properties on larger vertical scales does, in some places, suggest consistent signatures; however, a robust characterization is problematic for a number of reasons. The larger Fourier transform interval required to examine wave properties on large vertical scales implies that large-scale (geostrophic) flow structure as well as near-surface signatures at many stations contaminate the near-bottom wave signal. Further, structure with respect to depth versus height above bottom cannot be resolved. The relation between the predicted large-scale lee waves and the much shorter wavelength wave signals we analyze here is a subject of ongoing study. Energy transfer from the long lee waves to shorter internal waves, and in particular the coupling of near-inertial lee waves entering critical layer scenarios to high-frequency waves propagating in the opposite direction, is currently being investigated. For further details see Waterman et al. (2012, manuscript submitted to *J. Phys. Oceanogr.*).

We next apply linear wave radiation theory to bottom speed, stratification, and topography data to estimate the lee wave energy radiation. Lacking high-resolution multibeam data, we rely on the small-scale topographic parameters estimated by Nikurashin and Ferrari (2011), obtained from fitting a one-dimensional model spectrum to in situ one-dimensional topographic sections from all available ship soundings in the region from the U.S. National Geophysical Data Centre (NGDC). See Nikurashin and Ferrari (2011) for further details. The nature of the available topographic data implies that the topographic parameters required for the wave radiation calculation (namely the root mean squared height of the topography and the high-wavenumber slope) are estimated with a much coarser spatial resolution than the SOFine station sampled U_{bot}, N_{bot} and turbulent dissipation (see Fig. 1d), and the interpretation of the calculation's results should be considered keeping this in mind. We calculate the predicted lee wave energy radiation with the topographic data of Nikurashin and Ferrari (2011) and the observed bottom speeds and stratifications following the method of Nikurashin and Ferrari (2011), making all the assumptions therein. The results as a function of station are shown in Fig. 14.

The predicted lee wave energy radiation varies strongly (by 5 orders of magnitude) across the survey, ranging from ~ 0 to 175 mW m^{-2}. This variability is largely determined by the variability in the bottom speed, and to a lesser extent the bottom stratification: the largest radiated flux values are on the plateau where N_{bot} and U_{bot} are large, and inside the ACC jets where U_{bot} is large. The average value of the energy radiation for this latter group is 59 mW m^{-2}, more than 10 times

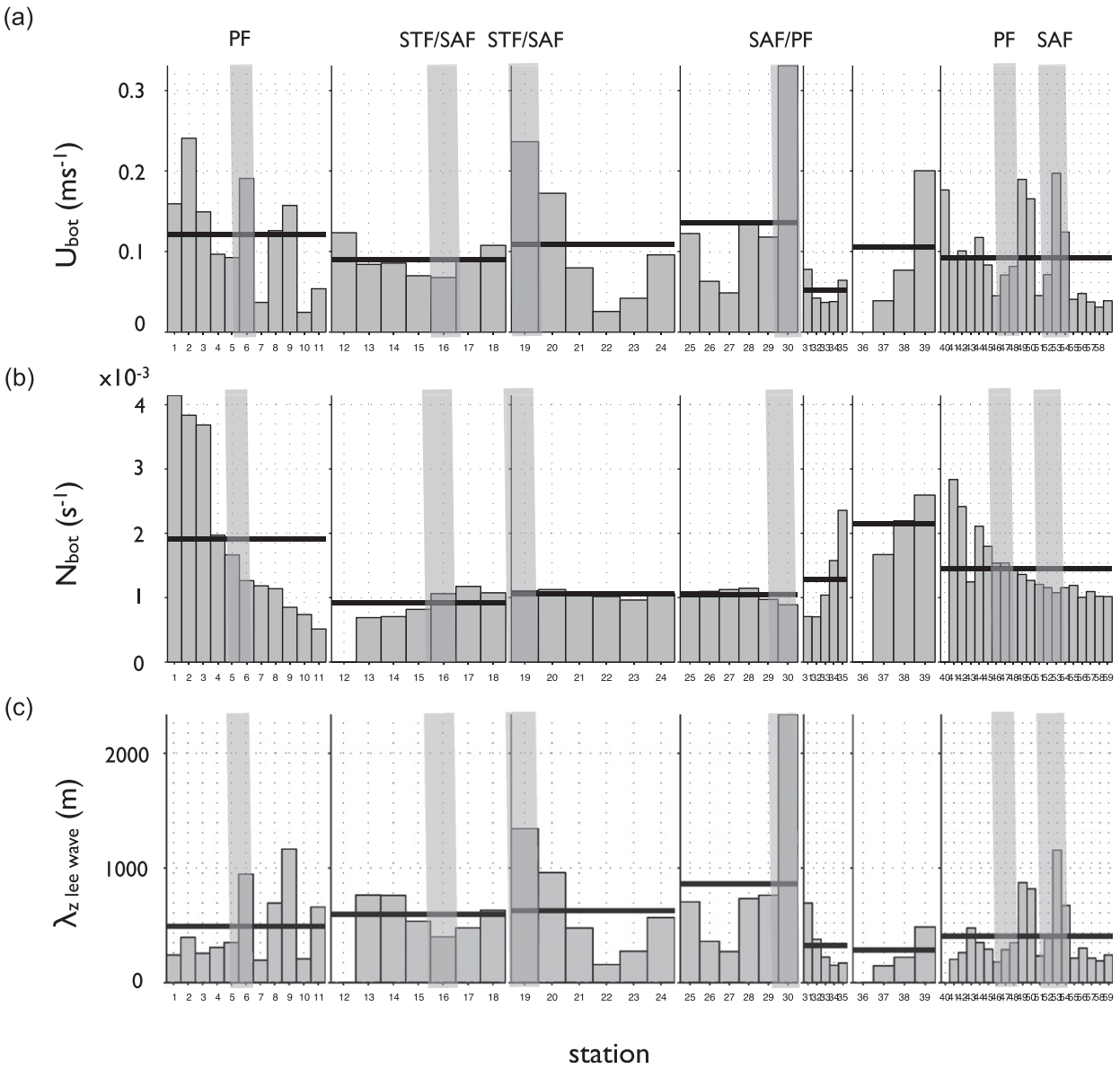

FIG. 13. (c) Lee wave vertical wavelength prediction as a function of station based on (a) observed near-bottom speed U_{bot}, and (b) buoyancy frequency (stratification) N_{bot}. Display is as in Fig. 5.

larger than the average value outside the ACC jets and off the plateau. In a transect-by-transect average sense, the predicted wave radiation tends to be smaller in the western half of the survey domain and larger in the eastern half, reflecting the larger values of topographic roughness that characterize the eastern part of the survey domain. These results are in many respects qualitatively similar to those of Nikurashin and Ferrari (2010b) for the Drake Passage and southeast (SE) Pacific regions. Here energy radiation was found to vary substantially across the fronts of the ACC and be dominated by the values inside the jets, and substantial differences in the energy radiation between the two regions arose from differences in topographic roughness. Quantitatively, the predicted energy radiation for the SOFine region lies in between the values characterizing the Drake Passage and SE Pacific, regions of high and low rates of abyssal mixing respectively: the overall SOFine regional-mean predicted radiation is 15 mW m^{-2} in contrast to 30 mW m^{-2} in the Drake Passage and 3 mW m^{-2} in the SE Pacific (Nikurashin and Ferrari 2010b). Characteristic values of topographic roughness in the 1–10-km wavelength range for the SOFine region also lie between those characterizing

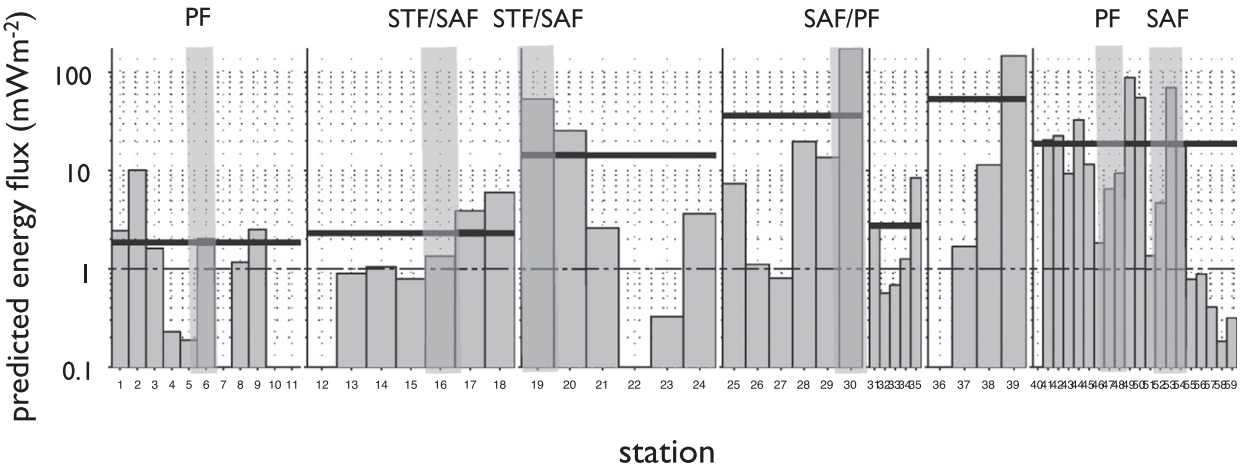

FIG. 14. Lee wave energy radiation prediction as a function of station based on observed near-bottom speed and stratification, and approximate topographic parameters. Display is as in Fig. 5.

the Drake Passage and SE Pacific regions [typical h_{rms} values are 10–40 m for the SOFine region versus 60–80 and 20–40 m for Drake Passage and the SE Pacific respectively (M. Nikurashin 2012, personal communication)]; however, our estimates of energy radiation are larger than those expected accounting for differences in topographic roughness alone (a factor 2 difference in h_{rms} between the SOFine region and Drake Passage suggest a factor four difference in energy radiation, whereas SOFine radiation estimates differ from those in Drake Passage only by a factor of 2). Estimates of energy radiation for the SOFine region are elevated by large bottom speeds, which tend to be order 50% larger than those that characterize Drake Passage [15–33 cm^{-1} inside jets for the SOFine region versus 10–20 cm^{-1} in the Drake Passage (Nikurashin and Ferrari 2010b)].

We compare the transect-average predictions of the radiated energy flux with the transect-average near-bottom depth-integrated dissipations from the microstructure measurements (Fig. 15). (The coarsely resolved topography data makes an individual station-by-station comparison impractical.) We note similar spatial trends in the two quantities: the predicted energy radiation and the near-bottom dissipation both are small along the western transect, highest along the eastern and central transects, and moderate in the deep waters along the northern boundary of the survey and in the shallow water on the eastern part of the plateau, trends that follow the general patterns of topographic roughness (Fig. 5c). In this way, these results are consistent with the qualitative conclusions of Nikurashin and Ferrari (2011), who find that wave radiation and subsequent breaking are very sensitive to the small-scale topographic roughness. Quantitatively, the transect-mean estimates of the predicted wave energy radiation range from 1.5 ± 0.9 mW m^{-2} in the west to 33 ± 21 mW m^{-2} along the central transect. These compare to estimates of the transect-mean depth-integrated dissipation in

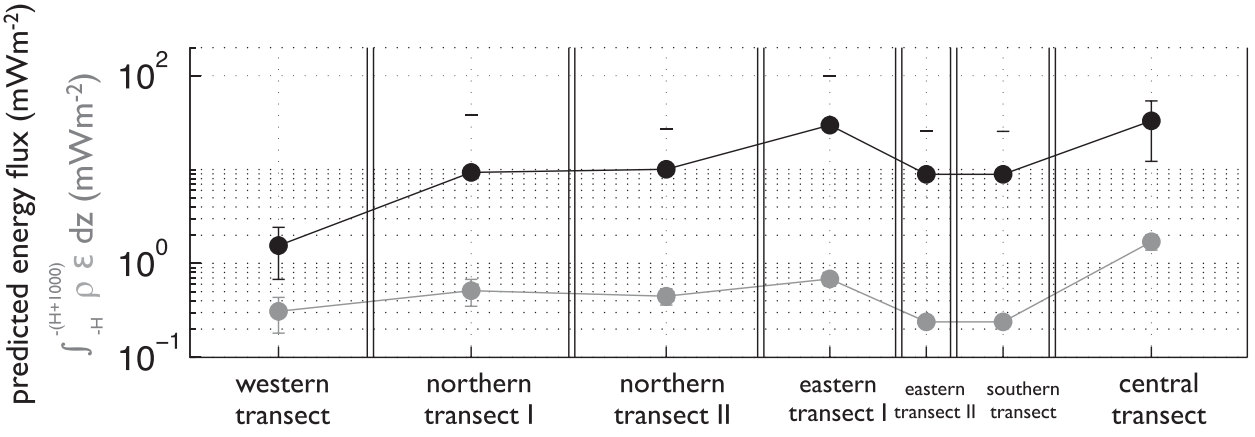

FIG. 15. A comparison of the transect-average predicted energy radiation (black) versus the transect-average depth-averaged power dissipated in the bottommost 1000 m from microstructure measurements (gray). Error bars denote the standard error in the mean.

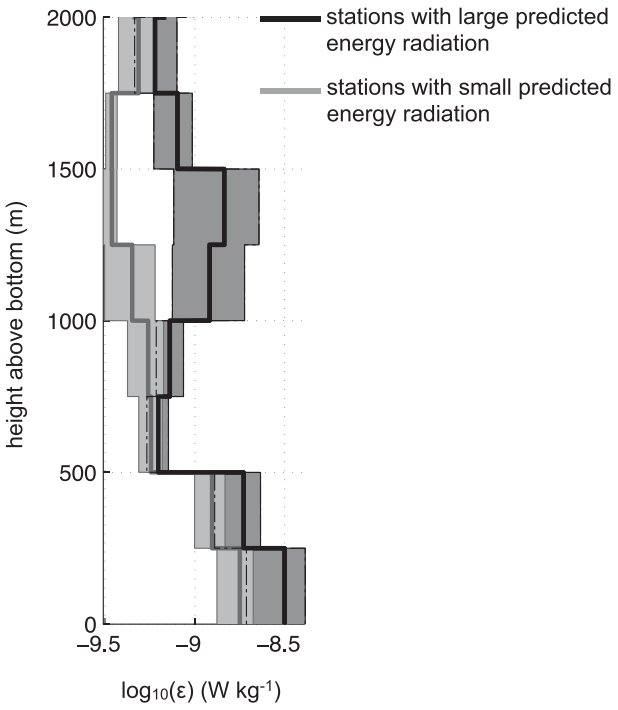

FIG. 16. Mean height profiles of ϵ contrasting stations with large predicted energy radiation (black) versus small predicted energy radiation (gray). Gray shading indicates the 90% confidence interval in the average vertical profiles calculated by bootstrapping.

the bottom kilometer from the microstructure survey measurements that range from 0.3 ± 0.1 mW m^{-2} in the west to 1.7 ± 0.3 mW m^{-2} along the central transect. On all transects, the dissipation in the bottom kilometer is found to be in the range of 2% to 20% of the predicted energy radiation, a much smaller fraction than the 50% found in the numerical simulations of Nikurashin and Ferrari (2010a, 2011). It should be noted however that the simulations apply to Drake Passage parameters, and the small steepness parameters $\epsilon_{\text{topo}} = (h_{\text{rms}} N_{\text{bot}})/(2\pi U_{\text{bot}})$ that characterize the SOFine region (a mean ϵ_{topo} value of 0.1 and a maximum value of 0.22) are expected to result in a more linear regime of wave radiation that produces less local dissipation.

As a final note we show the average height profiles of the microstructure measurements of turbulent dissipation for stations grouped according to the local prediction for internal wave energy radiation (Fig. 16). Here again the groupings are made on the condition of being greater or less than the regional mean value. The comparison highlights potentially significant differences in the near-bottom vertical profile of the turbulent dissipation rate for instances where internal lee wave generation is important versus where it is not. In both cases, ϵ is enhanced at the bottom and decays in the bottom kilometer. Average values in the bottom 1000 m are ~50% larger for the stations expected to have above-average lee wave radiation compared to those that are not. The most significant difference in the vertical profiles however is above 1000-m height above bottom, where the average height profile for stations predicted to have large internal wave energy radiation show a secondary local maximum centered around 1250–1500-m height. This is the same approximate height as the local off-bottom maximum observed in the average internal wave energy profile (Fig. 7c) and the average diffusivity profile (Fig. 4c) for stations showing enhanced near-bottom dissipation, and it is consistent with a convergence of internal wave energy flux that results from the background shear profile that characterizes stations with strong bottom flows (Fig. 11d). These signatures are suggestive of a critical layer fate for bottom-generated lee waves, and a consideration of the observational evidence of near-bottom critical layers that is tentatively suggested by these average profiles is currently underway to be reported on in future.

6. Discussion

In summary, the first systematic micro- and fine structure survey of the ACC confirms several of our expectations regarding the relationship between internal waves and turbulence in the Southern Ocean interior but challenges others. Amongst the former are included the following.

- Turbulent dissipation in the ocean interior appears to be underpinned by breaking internal waves (as evidenced by e.g., the correspondence of spatial patterns of ϵ and internal wave energy).
- We find evidence of enhanced turbulent dissipation and mixing associated with downward-propagating near-inertial waves in the upper approximately 1.5 km of the water column, suggestive of the anticipated role of wind generation of these waves in sustaining dissipation and mixing in the upper layers of the Southern Ocean. Depth-integrated dissipation rates in the upper 1500 m are O(1–10) mW m^{-2}, the same order as the estimates of the energy flux from the wind to near-inertial motions in the region by Alford (2001, 2003). We note that the observed levels of upper-ocean turbulent dissipation and inferred mixing are approximately an order of magnitude larger than those observed in the southeast Pacific during the Diapycnal and Isopycnal Mixing Experiment in the Southern Ocean (DIMES) (Ledwell et al. 2011), an enhancement consistent with the larger predicted energy flux from the wind to near-inertial motions in the region.
- We also find evidence of enhanced turbulent dissipation and mixing associated with upward-propagating, relatively high-frequency internal waves in the deep-

est 1–2 km of the water column that appear primarily in association with ACC jets flowing over small-scale topographic roughness. An interpretation of these waves as the (also anticipated) lee waves generated by geostrophic flow impinging on small-scale topography is supported by the qualitative match between the spatial patterns in predicted lee wave radiation and observed deep-ocean integrated dissipation.

However SOFine data also deliver some surprises. Despite all these aspects in which our results support expectations based on previous indirect work, we find that the enhancement of turbulent dissipation occurring at depth in association with ACC jet flow over small-scale topography is not as pronounced as expected from past finescale parameterization studies and lee wave radiation calculations. The near-bottom dissipation observed, typically of $O(1)$ mW m^{-2}, is about an order of magnitude smaller than estimates of dissipation from finescale parameterizations applied to observations (e.g., Naveira-Garabato et al. 2004; Kunze et al. 2006) and estimates of the rate of internal wave generation from wave radiation theory (Nikurashin and Ferrari 2010a,b; Scott et al. 2011), all of which are $O(10)$ mW m^{-2}. While the relatively modest enhancement of deep dissipation that we find compared to these studies may be due in part to the modest small-scale topographic variance in the SOFine region, we find that deep dissipation in our study area only accounts for a minor fraction (2–20%) of the predicted lee wave energy flux. Although in principle lee wave energy radiation does not have to match the depth-integrated dissipation, broad agreement was found in Drake Passage between the calculation of the radiated energy flux by Nikurashin and Ferrari (2010b) and observations of the local dissipation reported by Naveira-Garabato et al. (2004); however, it should be noted that the latter were derived from finescale measurements of internal wave shear and strain and not microstructure measurements. Hence our results pose some important questions. How good are our estimates of bottom energy generation and dissipation? If they can be trusted, where does the energy go?

Addressing the issue of confidence in our estimates of the bottom energy flux, we note that the quasi-stationary lee wave model has three inputs: 1) near-bottom stratification; 2) near-bottom ''background'' velocity; and 3) a topographic spectrum between horizontal scales λ_H defined by $U_{\rm bot}/N_{\rm bot} < \lambda_H < U_{\rm bot}/f$, where f is the inertial frequency. We are confident in our estimates of 1) and 2). We estimate the near-bottom background stratification using standard hydrographic data with in situ calibrations and exclude the small scales subject to sensor response issues. Further, the methods of adiabatic leveling and a simple, second-order least squares fit to the observed buoyancy frequency profile yield consistent results. Our estimates of 2) are derived from a standard LADCP configuration using the LDEO algorithm (Visbeck 2002). By incorporating bottom-track data, the Visbeck method makes the estimate of velocity in the bottom several hundred meters absolute and avoids the potential for errors in the near-bottom velocity arising from X-profile issues. For 3), ideally topographic parameters would be derived from in situ multibeam survey data; however, the quality of this data we collected under typical underway conditions made it unusable to define the topographic spectra required. Hence a strategic decision was made to use the coarse-resolution estimates of Nikurashin and Ferrari (2011). The topographic input imposes a limitation on the spatial resolution of our estimates of the radiated energy flux, hence the decision to discuss transect-mean values. Nevertheless, the topographic variables we input are small and plausible, and we believe them to be representative. We also note that even though our estimates of the energy flux are large compared to the observed depth integrated dissipation rates, they are not aphysically large and are similar to that contained in the GM spectrum.

On the other side of the equation is our estimates of dissipation from the microstructure measurements. The processing algorithms used on the microstructure measurements are those developed for the high-resolution profiler (Polzin and Montgomery 1996), modified to acknowledge the different sensor and noise characteristics of the VMP. Microstructure data were also processed using software provided by Rockland Scientific, manufacturers of the VMP. For further details see Waterman et al. (2012, manuscript submitted to *J. Phys. Oceanogr.*). The two methods return estimates of gradient variance that are consistent for signal levels in excess of the vibrational contamination. Further, we find that estimates of shear variance from the two independent probes are consistent, that the shear spectra are well resolved, and that the observed spectra agree with the Nasmyth spectrum characterizing high Reynolds number turbulence [see the appendix of Waterman et al. (2012, manuscript submitted to *J. Phys. Oceanogr.*) for a full discussion]. Based on all of these facts, we conclude that these estimates of turbulent dissipation are robust.

We suggest that the observed mismatch between estimates of energy generation and near-bottom dissipation should motivate thinking about alternative fates for the bottom-generated energy.

One possible explanation for the energy generation–energy dissipation mismatch is that a nonlocal balance applies: the energy generated propagates away and is

deposited elsewhere. Simulations of Nikurashin and Ferrari (2010a) and Nikurashin and Ferrari (2011) applicable to a Drake Passage–like regime, suggest that approximately 50% of the radiated energy is dissipated locally in the bottom 1000 m and 50% is radiated away to dissipate elsewhere. If all of the excess radiated energy was dissipated nonlocally, our estimates suggest that 80% or more of the generated energy flux radiates away and dissipates elsewhere. The radiation of a larger fraction of the energy generated is expected given the small steepness parameters that characterize the SOFine region; however, we question the applicability of such a nonlocal balance in this situation. Lee waves are ''compliant'' in the sense that their horizontal phase velocity is equal to the mean flow velocity at the bottom, and horizontal group velocities are generally smaller than the geostrophic velocity in the thermocline. They will thus be subject to $O(1)$ modifications of their wavenumber on a deformation scale.

An alternative fate is that energy is exchanged between the wave field and the mean flow through nonlinear wave–mean interactions. The rate of energy transfer is the rate of work, represented as the product of a momentum flux and appropriate mean gradient. To produce a mismatch between the bottom energy generation rate and the dissipation rate either (i) the waves break and deposit their momentum into the mean flow, or, (ii) wave momentum is transferred to the mean flow via nonlinearity. Both produce nominally the same result, but note that in the latter case, the waves do not need to dissipate. Our work suggests that the modest enhancement of deep dissipation seen in this region of the ACC relative to the predictions of fine structure and wave radiation studies may be, in some cases, understood in terms of nonlinear wave–mean flow interactions. The nature of those interactions and implications for the dynamics of the large-scale circulation will be discussed in a future publication.

Acknowledgments. The SOFine project is funded by the U.K.'s Natural Environmental Research Council (NERC) (Grant NE/G001510/1). The VMP-5500 was also purchased with this support. We thankfully acknowledge the support of Rockland Scientific International, especially for their timely advice delivered during the SOFine expedition. We are particularly grateful to all the scientists, technicians, officers and crew of the RRS *James Cook* for their hard work in making the SOFine cruise a very successful one. SW acknowledges the support of the Grantham Institute for Climate Change, Imperial College London. ACNG acknowledges the support of a NERC Advanced Research Fellowship (Grant NE/C517633/1). KLP acknowledges support from Woods Hole Oceanographic Institution bridge support funds. We thank Alex Forryan for processing the LADCP data in multiple ways. We thank Maxim Nikurashin for supplying the small-scale topographic data, and for his assistance with a number of concepts. Finally, we thank Eric Kunze for useful discussions.

APPENDIX

Internal Wave Integral Properties

a. Calculation

Internal wave properties discussed, namely, internal wave energy (Fig. 7), and R_ω and the polarization ratio (Fig. 10), each are calculated from the integration of the variance spectra of a quantity of interest between two specified vertical wavelengths. In each case the calculation of these integral properties shares the following common features.

(i) Fine structure (CTD and LADCP) profile data are segmented into half-overlapping vertical segments of length X dB. The choice of the segment length as well as the bin size of the data determine the number of points in the Fourier transform and restrict the possible range of vertical wavelength integration. They also set the vertical resolution of the resulting integral property profiles. For results presented here, $X = 512$ dB for CTD data and $X = 640$ dB for LADCP data resulting in 256 and 32 points respectively in each spectral calculation.

(ii) Segments are constructed both starting from the surface and the bottom. The near-surface integral property values are computed from the vertical segments defined starting from the surface, the near-bottom integral properties are computed from the vertical segments defined starting from the bottom, while interior values are computed by an average for top-down and bottom-up defined segments. In this way, each spectral calculation contains a full number of points.

(iii) The segmented data are detrended (by removing a linear fit) and windowed with a Hanning window of the same length as the data segment before Fourier transformation. The resulting spectra are compensated for the loss of variance by windowing and normalized so that the variance of the signal is equal to the integrated variance in the spectral domain.

(iv) Both shear and strain spectra are corrected for the loss of variance due to noncontinuous data, and in the case of the shear spectra, for high wavenumber attenuation associated with instrument limitations and data processing. Strain spectra are corrected

for bin-to-bin first differencing while the shear spectra are corrected for loss of variance because of 1) range-averaging, 2) finite differencing, 3) interpolation, and 4) instrument tilting. We ignore horizontal smoothing resulting from beam spreading which Polzin et al. (2002) found to be a minor effect. See Polzin et al. (2002) for further details. Integral properties are computed for both raw and corrected spectra, and the results reported are robust for both.

(v) In the case of LADCP profile data, spectra are computed for the downcast and upcast profiles separately then averaged before integration.

(vi) The spectra are integrated between $k_{\min} = 1/\lambda_{z\,\max}$ and $k_{\max} = 1/\lambda_{z\,\min}$ where $\lambda_{z\,\min}$ and $\lambda_{z\,\max}$ are the minimum and maximum vertical wavelengths of integration. These are selected to represent internal wave vertical scales and to avoid contamination by instrument noise at higher wavenumbers. See section b for a discussion on the choice of integration limits. In what follows, we use the notation of $\langle\rangle$ to indicate the integration of the spectra of the quantity indicated inside the brackets between these vertical wavelengths.

1) Internal wave energy

The spectrum of potential energy is computed from the Fourier transformation of height η given by

$$\eta = \frac{\Gamma - \Gamma_{\text{ref}}}{\dfrac{d\Gamma_{\text{ref}}}{dz}}.$$

Here Γ is neutral density and the reference subscript denotes a background value. Γ is computed from CTD profile data using the Commonwealth Scientific and Industrial Research Organisation (CSIRO) neutral density code. A background or reference value of Γ for each profile is approximated by a polynomial fit to the observed Γ "snapshot" consisting of a quadratic fit over overlapping segments of length 100 dB at the top of the profile with the segment length increasing by 4 dB every 8 dB. This results in a smooth fit to the observed neutral density profile. Here, $d\Gamma_{\text{ref}}/dz$ is then estimated by first differencing the Γ_{ref} profile over a window interval of 400 dB. Note that results are not particularly sensitive to the choices for the segment length or window interval provided they are reasonable. The integrated internal wave potential energy E_p is then computed as $E_p = 0.5\overline{N^2}\langle\eta^2\rangle$, where $\overline{N^2}$ is the segment mean buoyancy frequency.

The spectrum of kinetic energy is computed from the Fourier transformations of the horizontal velocities u and v (the zonal and meridional components respectively) from LADCP profile data. The integrated internal wave kinetic energy E_k is computed as $E_k = 0.5(\langle u^2\rangle + \langle v^2\rangle)$.

The total integrated internal wave energy is computed as the sum of the potential and (horizontal) kinetic energies: $E_{\text{tot}} = E_p + E_k$.

2) Shear and strain variance

Shear, the vertical gradient of the horizontal flow velocity, is calculated as the first difference of the horizontal velocity measured by the LADCP. Strain, a measure of the stretching and squeezing of isopycnals by internal waves, is calculated using the local relative change in buoyancy frequency from a background value $\zeta_z = (N^2 - N_{\text{ref}}^2)/N_{\text{ref}}^2$, where the buoyancy frequency N is calculated from the CTD measurements of temperature and salinity. It is computed with the CSIRO Seawater routines for MATLAB which is equivalent to adiabatic leveling over 6 dB. The background value N_{ref} is computed by applying the adiabatic leveling method of Bray and Fofonoff (1981) using a pressure range of 400 dB to calculate a reference N profile at each station.

Spectra of the buoyancy frequency normalized shear and strain are calculated as outlined above. We consider the observed variance in each normalized by that in the GM model spectrum (Munk 1981; Gregg and Kunze 1991), both integrated over the same wavenumber band, that is, $(\langle V_z^2\rangle/\overline{N^2})/(\langle V_{z\text{GM}}^2\rangle/\overline{N_0^2})$, where $N_0 = 5.24 \times 10^{-3}$ rad s^{-1}, the canonical GM buoyancy frequency, and $\langle\zeta_z^2\rangle/\langle\zeta_{z\text{GM}}^2\rangle$. The GM model spectrum and parameters are that of the GM76 model and as used in Kunze et al. (2006).

The integrated normalized shear and strain variance values normalized by the integrated GM model spectrum values in this way represent the energy density in the internal wave field in units of the GM energy density.

3) Shear to strain and the polarization ratios

The shear to strain variance ratio $R_\omega = \langle V_z^2\rangle/(\overline{N}^2\langle\zeta_z^2\rangle)$ is a measure of the internal wave field's aspect ratio and frequency content (Henyey 1991; Hughes and Wilson 1990; Polzin et al. 1995). We consider R_ω for both common and varying limits of integration for shear and strain variance (see the discussion on the sensitivity to the limits of integration below for further details). In the case of the former, R_ω is given simply by the definition above integrated over a common vertical wavenumber band. In the case of the latter in which the integration

range differs, we assume that both the shear and strain spectra have GM-like shapes over their respective integration bands, and we calculate the ratio of shear to strain variance with each normalized by the GM variance such that

$$R_\omega = 3\frac{\dfrac{\langle V_z^2\rangle}{\overline{N}^2}}{\dfrac{\langle V_{z\mathrm{GM}}^2\rangle}{\overline{N_0}^2}}\Bigg/\frac{\langle \zeta_z^2\rangle}{\langle \zeta_{z\mathrm{GM}}^2\rangle}.$$

The factor 3 corrects for

$$\frac{\dfrac{\langle \zeta_{z\mathrm{GM}}^2\rangle}{\langle V_{z\mathrm{GM}}^2\rangle}}{\overline{N_0}^2} = \frac{1}{3}.$$

We note that when shear and strain variance is considered for different wavenumber integration ranges, normalizing by GM variances over the appropriate respective wavenumber bands is crucial. However, if the gradient spectra do not have the same shape as the GM model, the relative contributions of shear and strain could be misrepresented.

The polarization ratio is the ratio of counterclockwise to clockwise polarized shear variance integrated over the vertical wavenumber band of interest. Its value relative to one indicates a dominance of counterclockwise or clockwise polarized shear, which has implications for the dominant direction of the energy flux of the sum of internal waves the variance is assumed to represent. A dominance of counterclockwise polarization (a polarization ratio > 1) indicates a dominance of downward directed internal wave energy propagation (in the Southern Hemisphere). Conversely a dominance of clockwise polarization (a polarization ratio < 1) indicates a dominance of upward internal wave energy flux.

4) ϵ_{fine}

We consider the dissipation rate predicted by observed internal wave properties and application of a finescale parameterization for the turbulent kinetic energy dissipation rate ϵ_{fine}. Its relation to the observed dissipation rate from microstructure measurements can give insight into the sources of variability that underpin the patterns of turbulent dissipation we observe. Here, ϵ_{fine} represents a parameterization of the turbulent kinetic energy dissipation rate associated with internal wave breaking that is applied to profiles of internal wave shear and density fine structure on vertical scales on the order of 100 m (see Polzin et al. 1995). It expresses the prediction for the dissipation rate in terms of the observed energy density and the energy density of the GM internal wave model (Gregg 1989) and includes both a dependence on the shear-to-strain ratio to account for the dominant frequency in the observed wave field (Polzin et al. 1995) and a dependence on latitude (Gregg et al. 2003):

$$\epsilon_{\mathrm{fine}} = \epsilon_0 \frac{\dfrac{\langle V_z^2\rangle}{\overline{N}^2}}{\dfrac{\langle V_{z\mathrm{GM}}^2\rangle}{\overline{N_0}^2}} h(R_\omega) L(\theta, N). \tag{A1}$$

Here $\epsilon_0 = 6.37 \times 10^{-10}$ and is a dimensionless energy level. The functions $h(R_\omega)$ and $L(\theta, N)$ account for the wave frequency and latitudinal dependence respectively. A comparison of ϵ from microstructure measurements versus ϵ_{fine} from a standard implementation of the parameterization [see Waterman et al. (2012, manuscript submitted to *J. Phys. Oceanogr.*) for details] is shown in Fig. A1. As the parameterization provides some temporal and spatial smoothing on subinertial flow scales, the correspondence of broad spatial patterns of the two fields suggests that observed patterns in the dissipation rate are likely underpinned by spatial variability or variability on subinertial time scales, as opposed to temporal intermittency on turbulent time scales.

b. Sensitivity to integration limits and other influences

The integral properties defined above can be very sensitive to the choice of the vertical wavelengths of integration, and it is important to understand the dependence of our results on the choice of integration limits. We consider three different sets of integration limits used by various authors in past studies of fine structure properties. These are as follows.

(i) A fixed range of integration limits common to both LADCP (E_k and shear) and CTD (E_p and strain) data.
(ii) A fixed range of integration limits with different ranges for LADCP and CTD data. The use of different integration ranges aims to avoid small scales where the LADCP data become noisy and large scales where strain variance is less likely to originate from internal waves, but requires normalizing by GM variances over the appropriate respective wavenumber bands. As such it assumes that the gradient spectra have the same shape as the GM model.

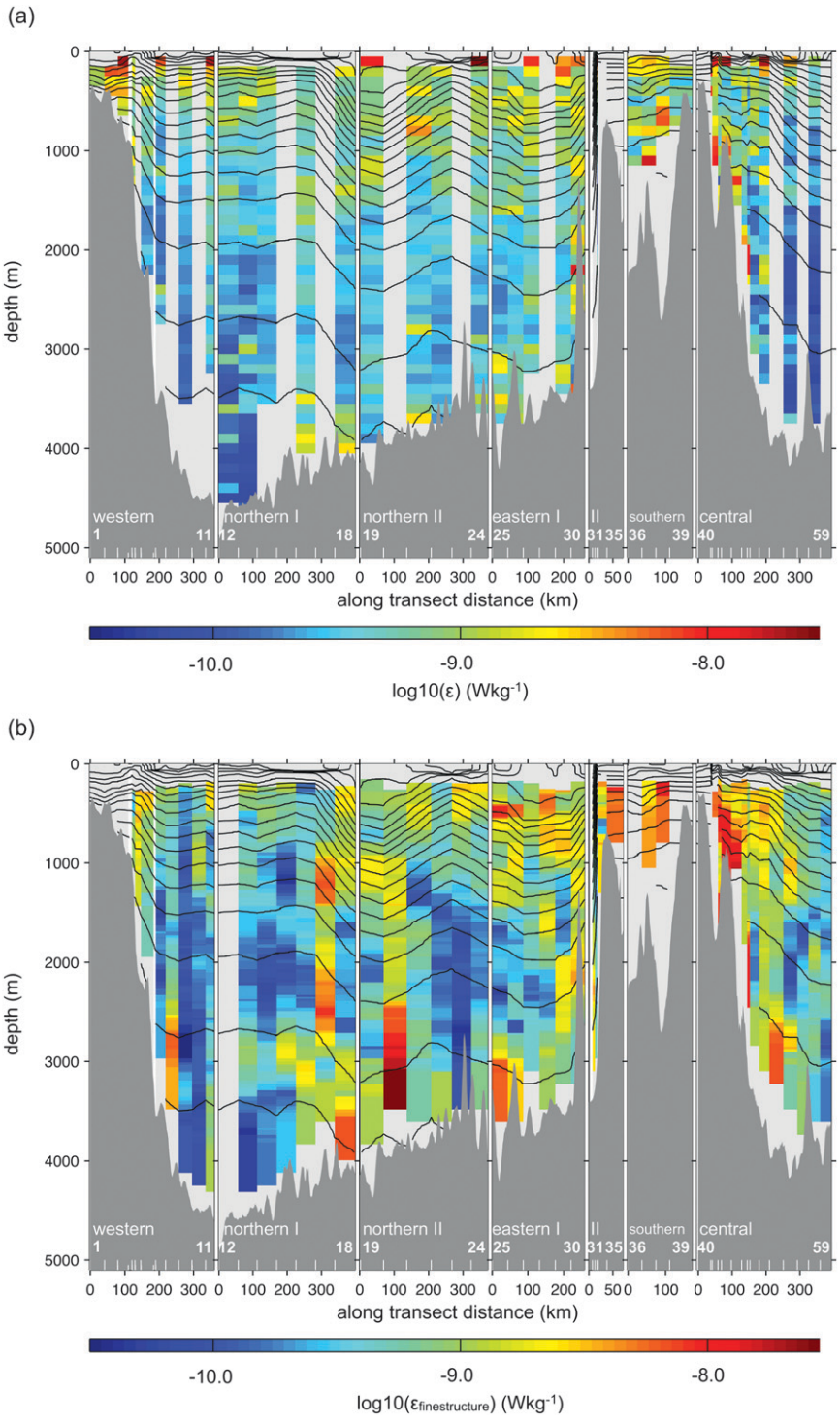

FIG. A1. A comparison of the microstructure observed turbulent dissipation rate and that predicted from finescale properties.

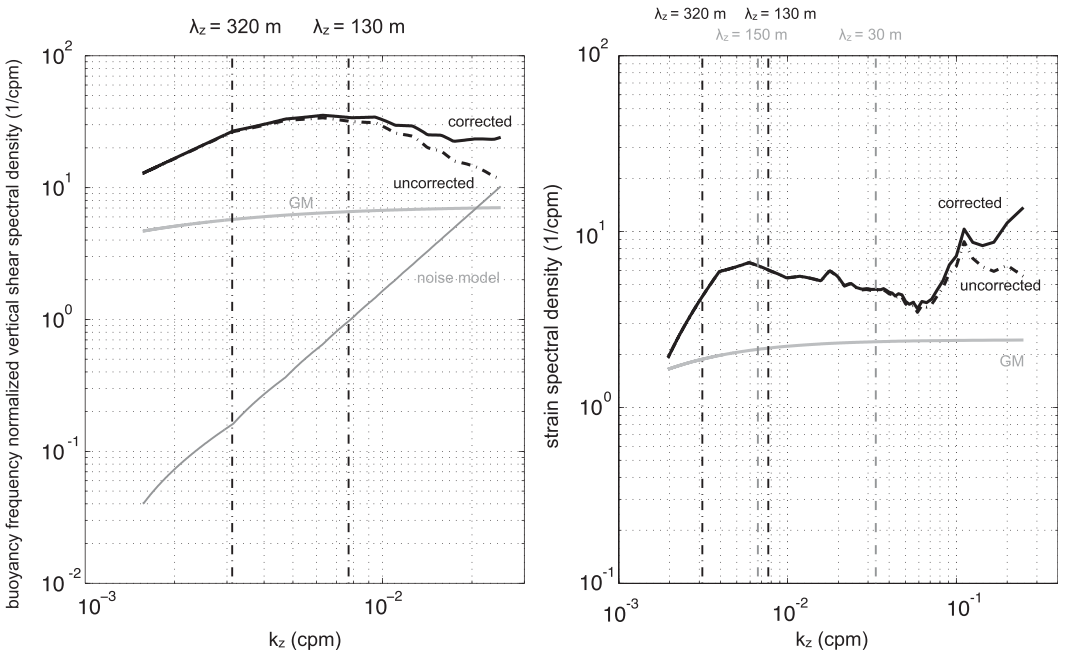

FIG. A2. The mean spectral shape for (left) buoyancy frequency normalized shear and (right) strain. The mean is of all depth bins for all stations. Both uncorrected and corrected average spectra are shown. These are compared to the GM model spectral shapes and, in the case of shear, the noise model spectrum of Polzin et al. (2002). The various vertical wavelengths of integration considered for the calculation of internal wave integral properties are indicated above.

(iii) Variable ranges of integration with different ranges for LADCP and CTD data and lower limits of integration determined by noise criteria.

In the case of (i) we choose very conservative (i.e., large) vertical wavelengths as the common limits of integration, namely $\lambda_{z\,\min} = 130$ m and $\lambda_{z\,\max} = 320$ m. As can be seen in Fig. A2, these limits are much larger than the short wavelengths where noise appears to impact the mean spectral variance levels. In the case of (ii), the choice of the shear and strain integration bandwidth is taken from Kunze et al. (2006): GM-normalized LADCP shear variances are integrated between vertical wavelengths of 130–320 m (to avoid instrument noise at smaller wavelengths) and GM-normalized CTD strain variances are integrated between vertical wavelengths of 30–150 m (to avoid contamination by background stratification from $\lambda_z > 150$ m). In the case of (iii), we apply different integration ranges for the LADCP and CTD data as in (ii), but in each case with a variable lower limit of integration decided on a spectra-by-spectra basis determined by a criterion based on noise considerations. In the case of the CTD data, as in Kunze et al. (2006) and following the concerns of Gargett (1990) about underestimating the internal wave variance if the spectrum becomes saturated at wavelengths $\lambda_z > 10$ m, we use a lower limit given by the shortest wavelength for which $\int_{\lambda_{\rm zmin}}^{150m} \Im(\zeta_z^2)(\lambda)\, d\lambda < 0.1$ (where $\Im$ denotes a normalized Fourier transform) or 10 m, using whichever is larger. In the case of the LADCP data, we consider the noise model of Polzin et al. (2002) using the number of pings averaged in each depth bin, and set the minimum wavelength of integration to 130 m or the minimum wavelength for which the noise spectral level is less than a critical ratio (taken to be 0.33 here) times the observed shear spectral level, again using whichever is larger.

The choice of integration limits does impact the value of the various integral properties computed however results discussed have been tested to be robust to all three ''industry standard'' configurations outlined above.

REFERENCES

Alford, M. H., 2001: Internal swell generation: The spatial distribution of energy flux from the wind to mixed-layer near-inertial motions. *J. Phys. Oceanogr.,* **31,** 2359–2368.

——, 2003: Improved global maps and 54-year history of wind-work on ocean inertial motions. *Geophys. Res. Lett.,* **30,** 1424, doi:10.1029/2002GL016614.

Bray, N. A., and N. P. Fofonoff, 1981: Available potential energy for MODE eddies. *J. Phys. Oceanogr.,* **11,** 30–46.

Efron, B., and G. Gong, 1983: A leisurely look at the bootstrap, the jackknife, and cross-validation. *Amer. Stat.,* **37,** 36–48.

Ferrari, R., and C. Wunsch, 2009: Ocean circulation kinetic energy: Reservoirs, sources, and sinks. *Annu. Rev. Fluid Mech.,* **41,** 253–282.

Furuichi, N., T. Hibiya, and Y. Niwa, 2008: Model-predicted distribution of wind-induced internal wave energy in the

world's oceans. *J. Geophys. Res.,* **113,** C09034, doi:10.1029/2008JC004768.

Gargett, A. E., 1990: Do we really know how to scale the turbulent kinetic energy dissipation rate ϵ due to breaking of oceanic internal waves? *J. Geophys. Res.,* **95** (C9), 15 971–15 974.

Gille, S. T., 1997: The Southern Ocean momentum balance: Evidence for topographic effects from numerical model output and altimeter data. *J. Phys. Oceanogr.,* **27,** 2219–2232.

Gregg, M. C., 1989: Scaling turbulent dissipation in the thermocline. *J. Geophys. Res.,* **94** (C7), 9686–9698.

——, and E. Kunze, 1991: Internal wave shear and strain in Santa Monica basin. *J. Geophys. Res.,* **96** (C9), 16 709–16 719.

——, T. B. Sanford, and D. P. Winkel, 2003: Reduced mixing from the breaking of internal waves in equatorial ocean waters. *Nature,* **422,** 513–515.

Henyey, F. S., 1991: Scaling of internal wave predictions for ϵ. *Dynamics of Internal Gravity Waves in the Ocean: Proc. Aha Huliko'a Hawaiian Winter Workshop,* Honolulu, HI, University of Hawaii at Manoa, 233–236.

Hughes, C. W., and C. Wilson, 1990: Observations of shear and vertical stability from a neutrally-buoyant float. *J. Geophys. Res.,* **95** (C10), 18 127–18 142.

—— and ——, 2008: Wind work on the geostrophic circulation: An observational study of the effect of small scales in the wind stress. *J. Geophys. Res.,* **113,** C02016, doi:10.1029/2007JC004371.

Kunze, E., 1985: Near-inertial wave propagation in geostrophic shear. *J. Phys. Oceanogr.,* **15,** 544–565.

——, E. Firing, J. M. Hummon, T. K. Chereskin, and A. M. Thurnherr, 2006: Global abyssal mixing inferred from lowered ADCP shear and CTD strain profiles. *J. Phys. Oceanogr.,* **36,** 1553–1576.

Ledwell, J. R., L. C. S. Laurent, J. B. Girton, and J. M. Toole, 2011: Diapycnal mixing in the Antarctic Circumpolar Current. *J. Phys. Oceanogr.,* **41,** 241–246.

Lumpkin, R., and K. Speer, 2007: Global ocean meridional overturning. *J. Phys. Oceanogr.,* **37,** 2550–2562.

Meredith, M., and N. Cunningham, 2011: Cruise report RRS *James Cook* JC054 (DIMES UK2). British Antarctic Survey Cruise Rep., 206 pp.

Munk, W., 1981: Internal waves and small scale process. *Evolution of Physical Oceanography,* B. A. Warren and C. A. Wunsch, Eds., The MIT Press, 264–291.

Naveira-Garabato, A. C., 2009: RRS *James Cook* Cruise 29, 01 Nov–22 Dec 2008. SOFine cruise report: Southern Ocean Finestructure. National Oceanography Centre Southampton Cruise Rep. 35, 216 pp.

——, K. Polzin, B. King, K. Heywood, and M. Visbeck, 2004: Widespread intense turbulent mixing in the Southern Ocean. *Science,* **303,** 210–213.

——, A. J. G. Nurser, R. B. Scott, and J. A. Goff, 2013: The impact of small-scale topography in the dynamical balance of the ocean. *J. Phys. Oceanogr.,* in press.

Nikurashin, M., and R. Ferrari, 2010a: Radiation and dissipation of internal waves generated by geostrophic flows impinging on small-scale topography: Theory. *J. Phys. Oceanogr.,* **40,** 1055–1074.

——, and ——, 2010b: Radiation and dissipation of internal waves generated by geostrophic motions impinging on small-scale topography: Application to the Southern Ocean. *J. Phys. Oceanogr.,* **40,** 2025–2042.

——, and ——, 2011: Global energy conversion rate from geostrophic flows into internal lee waves in the deep ocean. *Geophys. Res. Lett.,* **38,** L08610, doi:10.1029/2011GL046576.

Osborn, T., 1980: Estimates of the local rate of vertical diffusion from dissipation measurements. *J. Phys. Oceanogr.,* **10,** 83–89.

Polzin, K. L., 2010: Mesoscale eddy–internal wave coupling. Part II: Energetics and results from PolyMode. *J. Phys. Oceanogr.,* **40,** 789–801.

——, and E. T. Montgomery, 1996: Deep microstructure profiling with the High Resolution Profiler. *Proc. Microstructure Sensors Workshop,* Mt. Hood, OR, Office of Naval Research, 109–115.

——, and E. Firing, 1997: Estimates of diapycnal mixing using LADCP and CTD data from I8S. *International WOCE Newsletter,* No. 29, WOCE International Project Office, Southampton, United Kingdom, 39–42.

——, J. M. Toole, and R. W. Schmitt, 1995: Finescale parameterizations of turbulent dissipation. *J. Phys. Oceanogr.,* **25,** 306–328.

——, E. Kunze, J. Hummon, and E. Firing, 2002: The finescale response of lowered ADCP velocity profiles. *J. Atmos. Oceanic Technol.,* **19,** 205–223.

Scott, R. B., and Y. Xu, 2009: An update on the wind power input to the surface geostrophic flow of the world ocean. *Deep-Sea Res. I,* **56,** 295–304.

——, J. A. Goff, A. C. N. Garabato, and A. J. G. Nurser, 2011: Global rate and spectral characteristics of internal gravity wave generation by geostrophic flow over topography. *J. Geophys. Res.,* **116,** C09029, doi:10.1029/2011JC007005.

Sloyan, B. M., 2005: Spatial variability of mixing in the Southern Ocean. *Geophys. Res. Lett.,* **32,** L18603, doi:10.1029/2005GL023568.

Smith, W. H. F., and D. T. Sandwell, 1997: Global seafloor topography from satellite altimetry and ship depth soundings. *Science,* **277,** 1956–1962.

Sokolov, S. and S. R. Rintoul, 2009: Circumpolar structure and distribution of the Antarctic Circumpolar Current fronts: 1. Mean circumpolar paths. *J. Geophys. Res.,* **114,** C11018, doi:10.1029/2008JC005108.

Sparrow, M. D., K. J. Heywood, J. Brown, and D. P. Stevens, 1996: Current structure of the south Indian Ocean. *J. Geophys. Res.,* **101** (C3), 6377–6391.

Thompson, A. F., S. T. Gille, J. A. MacKinnon, and J. Sprintall, 2007: Spatial and temporal patterns of small-scale mixing in Drake Passage. *J. Phys. Oceanogr.,* **37,** 572–592.

Visbeck, M., 2002: Deep velocity profiling using lowered acoustic doppler current profilers: Bottom track and inverse solutions. *J. Atmos. Oceanic Technol.,* **19,** 794–807.

Watanabe, M., and T. Hibiya, 2002: Global estimates of the wind-induced energy flux to inertial motions in the surface mixed layer. *Geophys. Res. Lett.,* **29,** 1239, doi:10.1029/2001GL014422.

Wu, L., Z. Jing, S. Riser, and M. Visbeck, 2011: Seasonal and spatial variations of Southern Ocean diapycnal mixing from Argo profiling floats. *Nat. Geosci.,* **4,** 363–366.

Wunsch, C., 1998: The work done by the wind on the oceanic general circulation. *J. Phys. Oceanogr.,* **28,** 2331–2339.

Zika, J. D., B. M. Sloyan, and T. J. McDougall, 2009: Diagnosing the Southern Ocean overturning from tracer fields. *J. Phys. Oceanogr.,* **39,** 2926–2940.